PHOTONICS INSIGHTS

# Integrated photonic spectrometers: a critical review

**Maarten R. A. Peters,[a] Diana Mojahed,[a] Wenchao Ma,[b] Raphaël Pestourie,[c] Tian Gu,[a] Steven G. Johnson,[d] and Juejun Hu[a,*]**

[a]Department of Materials Science and Engineering, Massachusetts Institute of Technology, Cambridge, USA
[b]Department of Chemistry, Massachusetts Institute of Technology, Cambridge, USA
[c]School of Computational Science and Engineering, Georgia Institute of Technology, Atlanta, USA
[d]Department of Mathematics, Massachusetts Institute of Technology, Cambridge, USA

**Abstract.** Integrated photonics, where optical components are fabricated on a chip-scale platform leveraging standard microfabrication technologies, has transformed telecommunications and data communications, quantum optics, and molecular sensing. Optical spectrometry is yet another field that integrated photonics is poised to revolutionize. Unlike traditional bulky, costly benchtop spectrometers, integrated photonics promises miniaturized, rugged, and low-cost spectrometer-on-a-chip modules with broad application prospects ranging from communications to medical imaging. In this review, we survey the various designs of integrated photonic spectrometers through the lens of their underlying operating principles, aiming to reveal quantitative performance scaling laws that transcend specific implementations. This approach enables a general, physically grounded comparison of spectrometer capabilities without being bogged down by device-level details. We further provide guidance on selecting appropriate spectrometer architectures for different applications, taking into account not only their reported advantages but also the practical limitations and implementation challenges.

Keywords: integrated photonics; waveguide; spectrometry; spectroscopy.

Received May 8, 2025; revised manuscript received Aug. 6, 2025; accepted Oct. 8, 2025; published online Nov. 7, 2025.



[DOI: 10.3788/PI.2025.R10]



*Address all correspondence to Juejun Hu, hujuejun@mit.edu

## 1 Introduction

Optical spectrum analysis is the cornerstone of spectroscopic sensing, optical network performance monitoring, hyperspectral imaging, astronomical spectroscopy, and spectral domain optical coherence tomography (SD-OCT). Such analysis traditionally involves bulky and costly benchtop instruments only found in dedicated laboratories. Emerging market opportunities ranging from point-of-care diagnostics to sensor network deployment are now increasingly demanding spectrometers with reduced size, weight, power, and cost (SWaP-C) metrics.[1–4]

Photonic integrated circuits (PICs),[5–9] the optical analog of electronic integrated circuits, offer a promising route towards miniaturized spectrometers. Compared to conventional spectrometers based on bulk optics, PIC technologies promise several critical performance advantages in addition to their apparent SWaP-C benefits. Photonic integration defines devices on-chip with lithographic precision, thereby largely obviating the need for stringent alignment between discrete optical elements and dramatically boosting the ruggedness of spectrometer modules. The advent of ultralow-loss optical waveguides[10] allows long optical paths to be folded onto a small chip, enabling spectrometers with exceptional spectral resolution. PICs also provide access to ultra-compact, high-speed optical switches to route light between different paths through thermo-optic (TO), electro-optic (EO), or micro-electromechanical systems (MEMS), an essential feature for time-domain modulated spectrometers.[11] Finally, PICs facilitate interfacing with other chip-scale micro-modules such as electronics for signal processing and microfluidics for analyte handling, potentially leading to full system-in-a-package solutions.

In this review, we aim to provide a comprehensive survey of the state-of-the-art in PIC-based spectrometers. The review is organized as follows. We will start with describing a generic model of optical spectrometers, followed by an overview of the spectrum reconstruction methods. Next, we will proceed to review different variants of PIC-based spectrometer designs and assess their relative merits. Given the focus on PIC technologies, we limit the scope of this review to waveguide-based spectrometers, and we direct interested readers to other reviews that cover non-PIC spectrometers (which may still leverage chip-scale microsystem technologies).[12–17] Beachhead markets where PIC-based spectrometers are likely to make a disruptive impact are then evaluated.

## 2 Generic Model of Optical Spectrometers

In its generic incarnation, a spectrometer is a linear optical device involving a set of photodetectors, each with distinct spectral responses (Fig. 1). The different spectral responses are customarily defined by optical filters concatenated with the detectors. The photodetectors can be a spatial array of detector pixels, or a single-pixel detector integrated with a time-varying filter, effectively creating a time-domain sequence of the detector set (or

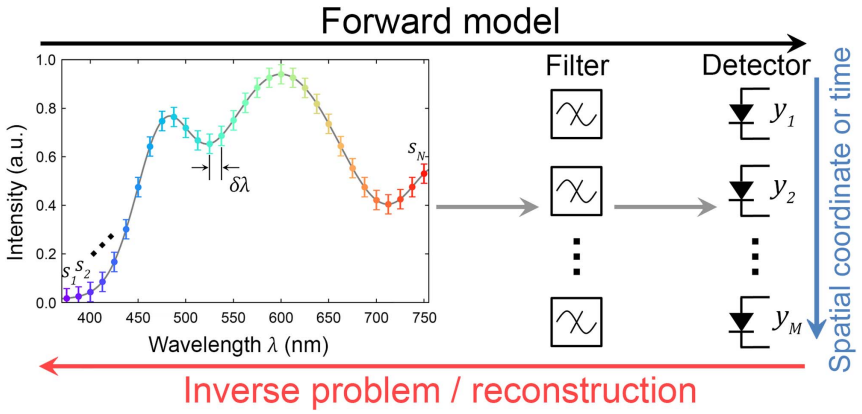


**Fig. 1** Generic model and inverse problem for an optical spectrometer comprising a set of photodetectors coupled to optical filters. To numerically describe the spectrometer, the input spectrum is approximated by intensities $s_j$ at a set of discrete wavelengths $\lambda_j$. The photodetectors collect signals $y_i$, which are used to reconstruct the input spectrum.

some combination of the two configurations). This distinction defines two major classes of optical spectrometers: classical dispersive spectrometers based on prisms or gratings are examples of the former configuration, whereas Fourier-transform infrared (FTIR) spectrometers epitomize the latter time-domain modulated design.[11]

The wavelength-dependent optical transmittance for each of the detectors is denoted by $T_i(\lambda)$, where $\lambda$ is the wavelength and $i$ denotes the detector number in either the spatial- or time-domain. The index $i$ takes a value between 1 and the number of measurements $M$. The signal intensity on the $i$th detector is therefore

$$I_i = \int R_i(\lambda)T_i(\lambda)S(\lambda)\mathrm{d}\lambda + \eta_i, \tag{1}$$

where $R_i(\lambda)$ denotes the responsivity of the photodetector, $S(\lambda)$ gives the input spectrum or more specifically the power spectral density of the input signal received through the spectrometer's input aperture, and $\eta_i$ is the noise at the $i$th detector.

In order to reconstruct the input spectrum, it is customary to discretize over a discrete set of wavelength points $\lambda_j$, with $1 \le j \le N$, where $N$ is the spectral channel count. Equation (1) can then be approximated as a weighted sum at these discrete wavelength points $\lambda_j$ (a quadrature rule[18–20]):

$$I_i = \sum_j w_j R_i(\lambda_j)T_i(\lambda_j)S(\lambda_j) + \eta_i \quad \Leftrightarrow \quad y = Gs + \eta, \tag{2}$$

where on the right, we have expressed the weighted sum in a matrix form: $y$ is the column vector with $I_i$ as its elements, the elements of column vector $\eta$ represent the noise at each detector, the column vector $s$ has length $N$ and contains the power spectral density at each wavelength $\lambda_j$, and $G$ is a matrix with entries $G_{ij} = w_j R_i(\lambda_j)T_i(\lambda_j)$ (analogous to the "point spread function (PSF) matrix" in imaging). The simplest quadrature rule is a Riemann sum, with equally spaced $\lambda_j = \lambda_0 + j\delta\lambda$ and equal weights $w_j = \delta\lambda$.[21,22]

Discretizing the integral into a finite number of points $\lambda_j$ is closely related to discretizing the unknown spectrum $S(\lambda)$ into a finite vector $s$ of discrete $S(\lambda_j)$ samples. Given these samples $S(\lambda_j)$, one must then interpolate them somehow to obtain $S(\lambda)$. In fact, the choice of quadrature scheme usually implicitly defines a corresponding interpolation: Riemann sums correspond to piecewise constant interpolation, a trapezoidal rule[18–20] corresponds to piecewise linear interpolation, and more sophisticated schemes like Gaussian quadrature or Clenshaw–Curtis quadrature[19,20] correspond to higher-order polynomial interpolants (from carefully chosen, unequally spaced points $\lambda_j$). Alternatively, one could explicitly expand $S(\lambda) \approx \sum_\ell b_\ell(\lambda)x_\ell$ in some finite set of basis functions $b_\ell$ (e.g., polynomials and radial basis functions[23] such as Gaussians[24–26]) and unknown coefficients $x_\ell$. The matrix equation and the spectrum vector in Eq. (2) can be expressed in terms of this basis:

$$y \approx Ax + \eta, \qquad A = GB, \qquad s \approx Bx, \tag{3}$$

with $B$ a matrix with elements $B_{j\ell} = b_\ell(\lambda_j)$ and $x$ a column vector of length $L$ composed of $x_l$.

Even more generally, $S(\lambda)$ could be expressed as a nonlinear function of unknown coefficients, such as some type of neural network[27–33]—this complicates the reconstruction problem by making it nonlinear and nonconvex, so we focus on linear models $Ax$ in this review.

Setting $B$ to an identity matrix yields $x = s$ and makes the matrix equation for $y$ in Eq. (3) identical to that in Eq. (2). This is, for example, the case for classical dispersive spectrometers, where there is a one-to-one correspondence between wavelength and detector pixel and thus the matrices $A$ and $G$ are square. For classical dispersive spectrometers with low crosstalk, $A$ and $G$ can be well approximated as diagonal matrices whose diagonal elements are determined by the wavelength-dependent insertion loss and detector responsivity.

In the case of a square matrix $A$, $x$ may be inferred straightforwardly by inverting $A$. When the matrix $A$ is not square, e.g., because the number of detector pixels $M$ is not equal to the number of wavelength points $N$ (and $B \notin \mathbb{R}^{N\times M}$), Eq. (3) is either over- or underdetermined and the inverse reconstruction task becomes a problem of linear algebra and optimization. In the following section, we will treat this optimization problem in more detail before moving on to discuss the performance metrics of spectrometers.

## 3 Spectrum Reconstruction

Previously, we noted that $A$ becomes a square matrix when the spectrum coefficient vector $x$ and the measurement vector $y$ have the same number of elements. In this case, $x$ could be estimated as $\hat{x} = A^{-1}y$. There are two complications. First, the presence of noise means that one must be concerned with the "conditioning" of the matrix $A$:[34] if $A$ is close to singular ("ill-conditioned"), then the solution can be very sensitive to noise. For an ill-conditioned $A$, different spectra $x$ can yield nearly the same measurements $y$ and will be impossible to distinguish once noise is added. This issue is addressed by (1) designing the optics to yield a well-conditioned $A$ (different input spectral components should form very different intensity patterns on the detector array) or related figures of merit for the inference error, through, e.g., inverse design[35] or "end-to-end" optics/inference co-design;[36–43] and/or (2) adding regularizations based on prior knowledge.[44–52] The second complication is that, in practice, $A$ will often be non-square: it is either overdetermined (more measurements than unknowns) or underdetermined (more unknowns than measurements, which also requires additional prior knowledge). We discuss the over/underdetermined situations in more detail below.

### 3.1 Overdetermined Reconstruction

A straightforward approach to overdetermined reconstruction solves the least squares[53,54] to find the coefficients:[55–59]

$$\hat{x} = \arg\min \|Ax - y\|_2^2. \tag{4}$$

If the basis functions are nonnegative, one may also wish to impose the constraint $x \succeq 0$ (i.e., all elements of $x$ are nonnegative) in order to ensure that the reconstructed spectrum is nonnegative at all frequencies. In many cases, however, we have found that this additional constraint seems to be unnecessary to obtain a nonnegative spectrum, and we omit it below. Least-squares problems, with or without nonnegativity constraints (and other variations such as weighting for unequal or correlated noise between different sensors), are convex quadratic optimization problems that can be solved by many well-known efficient algorithms.[54,60–62]

To mitigate vulnerability to noise, one may trade off model error $\|Ax - y\|_2$ for denoising. A common practice is Tikhonov regularization (also known as ridge regression):

$$\hat{x} = \arg\min_x \|Ax - y\|_2^2 + \alpha\|x\|_2^2, \tag{5}$$

where $\alpha \geq 0$ is a regularization coefficient[44–46] and the term $\alpha\|x\|_2^2$ penalizes the magnitude of the reconstructed spectrum. More generally, the regularization term can be written as $\alpha\|\Phi x\|_2^2$, with $\Phi$ being a matrix chosen according to prior knowledge of the spectrum and the features that should be suppressed or enhanced. Two or more regularization terms may be used simultaneously,[63] including terms with other norms such as the $L_1$ norm discussed below [Ref. [57] used L1 regularization, similar to Ref. [50] (private communications with Hui Cao, 2024)]. Ideally, Eq. (5) requires the noise $\eta$ on each detector to be identical and uncorrelated. If the requirement is not satisfied, Eq. (5) may still be applicable, while a corrected version of Eq. (5) may be available given sufficient knowledge about the noise.[64] A regularization trade-off very similar to Tikhonov is achieved by a truncated singular value decomposition (discarding singular values of $A$ below some threshold),[58,65] which is related to principal component regression.[66]

### 3.2 Underdetermined Reconstruction

In an underdetermined inverse problem (reconstructing more unknowns $x$ than measurements $y$), infinitely many solutions exist. Although one may still use Tikhonov regularization for reconstruction and denoising, prior knowledge about the measured spectrum is generally needed for meaningful reconstruction.

As a simple example, if we assume that the spectrum consists only of a few bright peaks/lines in a dark background, or perhaps comprises a few spectral patterns out of a large set of possibilities, so that the solution $\hat{x}$ is "sparse" (mostly zero) in an appropriate basis, the well-known techniques of "compressed sensing" can be applied.[47–52] The most common such technique is least squares with $L_1$ regularization (also called LASSO, for "least absolute shrinkage and selection"):[67,68]

$$\hat{x} = \arg\min_x \|Ax - y\|_2^2 + \alpha\|x\|_1, \tag{6}$$

where $\|x\|_1 = \sum_j |x_j|$ penalizes non-sparse solutions with penalty strength $\alpha \geq 0$. There are many variations on this idea; e.g., if one also adds a Tikhonov ($L_2$) regularization, it is called an "ElasticNet".[68] A key point is that all of these variants are still convex problems with many efficient solution algorithms.[60,62] Hyperparameters are sometimes determined with the help of validation against additional data not used for training/fitting.[69–71]

Recall from Eq. (3) that $x$ contains the expansion coefficients of the spectrum $S(\lambda)$ in a basis described by $B$ (also called a dictionary in compressed sensing). Unlike the overdetermined case, the basis here may be overcomplete (i.e., $B$'s columns may be linearly dependent).[72] The sparseness of $x$ relies on the choice of $B$. If prior knowledge about an appropriate $B$ is unavailable or insufficient, the optimization can include the basis $B$ itself in the optimization parameters, as in "dictionary learning".[72,73]

Other machine-learning methods have also been used, especially in the related problem of imaging,[74–76] in which neural networks provide nonlinear regularization and reconstruction. These techniques have the advantage that they can learn to reconstruct spectra that are similar to a given training set, even if the characteristics of the training data are not easily described by a simple formula such as those involving $L_2$ or $L_1$ regularization. Their disadvantage is that a much larger training set is typically required, and it is often unclear how well the resulting algorithm and trained parameters will generalize to new out-of-sample data.[77,78]

In the succeeding sections, we will discuss various types of PIC-based spectrometers. The discussion focuses on the performance metrics that relate to the spectral features, including the spectral channel count $N$, i.e., the number of data points comprising the optical spectrum, spectral resolution $\delta\lambda$, characterizing the minimum resolvable wavelength spacing between the data points (Fig. 1), and bandwidth $\Delta\lambda$, the operational wavelength range of the spectrometer, which is classically given by the product of $N$ and $\delta\lambda$ when the wavelength points are roughly equally spaced. Metrics related to the signal-to-noise ratio (SNR) are separately discussed in Sec. 8.

## 4 Spatially Dispersed On-Chip Spectrometers

In this part of the review, we discuss the different types of on-chip spectrometers that have been proposed. We first consider spatially dispersed spectrometers, where the spectral response is spread out in space (Fig. 1). We distinguish four categories of spatially dispersed spectrometers, i.e., classical dispersive spectrometers, resonator array spectrometers, wavelength multiplexing spectrometers, and stationary-wave integrated Fourier-transform spectrometers.

### 4.1 Classical Dispersive Spectrometers

In a classical dispersive spectrometer, the incident light is split into different spectral components using a dispersive element, such as a grating, prism, or hologram. Each of these components is then captured using detectors in an array to give the optical spectrum. For a well-designed classical dispersive spectrometer with low optical crosstalk, the signal at each detector $y_i$ thus directly correlates to spectral intensity $s_i$ (at wavelength $\lambda_i$). Most on-chip implementations of such spectrometers make use of planar waveguide gratings, in particular echelle gratings [Fig. 2(a)][79–88] or arrayed waveguide gratings [AWGs, Fig. 2(b)].[80,81,89–93] Other approaches include photonic crystal (PhC) gratings,[94] digital planar holograms,[95,96] PhC superprisms[97], and in-plane metalenses.[98]

Let us now have a look at the performance metrics (Table 1). The scaling behavior of $N$ and $\delta\lambda$ is important for on-chip integration. For classical spectrometers, the spatial separation between wavelengths scales with the optical path length (OPL) between the dispersive element and the detector array. In other words, both the spectral channel count and resolution improve linearly with the OPL and most likely also scale linearly with the geometric dimensions of the spectrometer. Consequently, on-chip classical dispersive spectrometers typically suffer a performance loss compared to their benchtop counterpart.

The next metric we discuss is the operating bandwidth $\Delta\lambda$. Consider a very broadband signal incident on a grating or other dispersive element. Due to the emergence of different diffraction orders, different wavelengths can couple into the same output channel. The free spectral range (FSR) is defined as the spacing

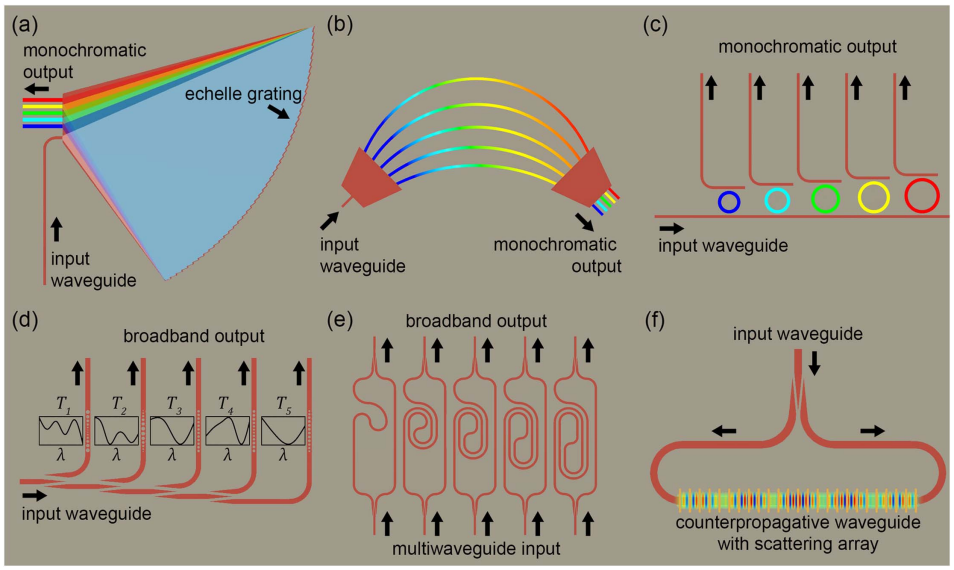


**Fig. 2** Schematic representations of the types of spatially dispersed on-chip spectrometers. (a) Classical dispersive spectrometer based on an echelle grating. (b) Classical dispersive spectrometer based on an arrayed waveguide grating. (c) Resonator array spectrometer comprised of microring resonators. (d) Wavelength multiplexing spectrometer based on a broadband filter array. Examples of (uncorrelated) transmission spectra $T_i$ are plotted next to each filter. (e) Stationary Fourier-transform (FT) spectrometer with multiple input waveguides. (f) Stationary-wave integrated Fourier-transform spectrometer (SWIFTS) in the counterpropagative configuration. A prototypical standing wave electric field profile is plotted in the SWIFTS.

between two consecutive wavelengths that are coupled into the same spectral channel (Fig. 3). The maximum $\Delta\lambda$ of the spectrometer is determined by this FSR. The FSR is determined by the design of the dispersive element, e.g., for a grating, the FSR is inversely proportional to the diffraction order $m$. To increase the operating bandwidth in echelle gratings, neighboring diffraction orders can be suppressed by specifically engineering each individual grating facet.[79] Another strategy to extend the bandwidth of the spectrometer (Table 1) is cascading dispersive elements.[93,126] First, a low-resolution dispersive element splits the broadband light into multiple wavelength bands. Then, a second set of elements splits each band into the high-resolution optical channels (where high resolution refers to small $\delta\lambda$). Finally, we note that for some dispersive elements, such as an AWG, a trade-off arises between bandwidth and resolution. This trade-off results from a decrease in both $\delta\lambda$ and the FSR when the optical path length difference (OPD) between the waveguides in the AWG increases (for fixed free propagation regions).

Finally, we discuss the influence of fabrication imperfections. In classical dispersive spectrometers, such imperfections generally result in optical crosstalk, i.e., the spillover from one wavelength into the neighboring spectral channels. When it comes to arrayed waveguide gratings, the crosstalk is usually induced by the non-uniformity of the waveguides across the linear waveguide grating. This non-uniformity is usually caused by variation in waveguide width across the chip, leading to a distortion of the wavefront compared to the design.[127] For echelle gratings, as well as other grating-based or holographic spectrometers, the light propagates through a slab waveguide, rather than a strip waveguide. In this case, width variations do not pose an issue, and the device generally exhibits less optical crosstalk.[86] Optical crosstalk in this case arises from inaccurate placement and size variation in the grating or PhC elements[85] or from non-uniformity in the thickness of the waveguide layer.

### 4.2 Resonator Array Spectrometers

The second approach to spatially dispersed on-chip spectrometers uses optical resonator arrays. In this case, each resonator will be tuned to a different resonant wavelength [Fig. 2(c)]. So, when a broadband signal comes in, each resonator will now split off a spectral component and funnel it into a photodetector. Proposed types of resonators include microdonut or microring resonators (MRRs)[99,101,128] and PhC cavities.[100,129] One advantage of such a design is that the spectral resolution is not directly limited by the physical size of the optical components. Instead, $\delta\lambda$ is determined by the quality factor $Q$ of the resonator. On-chip resonators can achieve very high $Q$, allowing for compact spectrometers with a high spectral resolution (small $\delta\lambda$) and a small footprint (Table 1).

Similar to the classical dispersive spectrometers, the bandwidth of the device is limited by the FSR of the resonator (Fig. 3). Furthermore, there still is a linear scaling behavior, but it now applies to $N$. Each resonator corresponds to one spectral channel or wavelength, so for a large $N$, a large resonator array is needed.

For some resonators, e.g., MRRs, the trade-off between bandwidth and resolution is also present.[130] This trade-off results from the scaling of the performance metrics with the radius $R$ of the MRR. The FSR of the resonator increases as we reduce $R$. The quality factor on the other hand depends on the optical loss in the resonator. When the bending loss exceeds the other

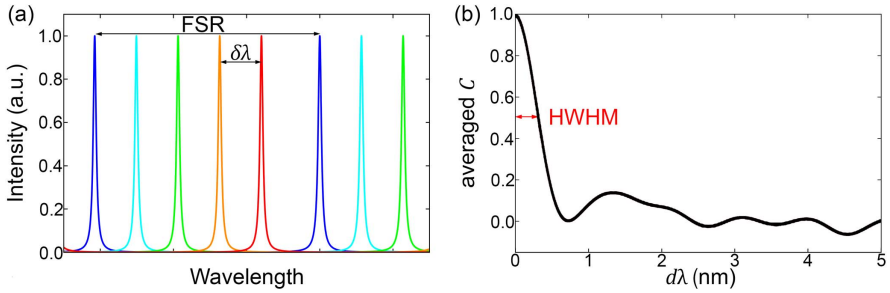


**Fig. 3** (a) Each color represents the transmission into one spectral channel of a spectrometer based on a classical dispersive element or resonator array. Wavelengths separated by the FSR of the dispersive element are collected by the same detector. (b) Typical example of the averaged spectral correlation function [Eq. (7)] as a function of wavelength spacing. The spectral resolution relates to the half-width at half-maximum (HWHM) of the curve.

sources of optical loss in the MRR, the reduction of $R$ and thus an increase in FSR is accompanied by an increasing loss, thus reducing $Q$ and increasing $\delta\lambda$. Therefore, bending loss sets a practical limit to size downscaling of MRR-array-based spectrometers.

Fabrication imperfections, such as sidewall roughness and variation in waveguide dimensions, influence the resonator array spectrometers in two ways. Firstly, fabrication imperfections introduce losses that decrease the quality factor of the resonator, resulting in increased crosstalk or reduced resolution of the device. Secondly, imperfections result in reduced control over the resonant frequency of individual resonators and again increased crosstalk between the channels. The second issue, however, can potentially be mitigated by active tuning of the resonant frequencies at the expense of device complexity.

### *4.3 Wavelength Multiplexing Spectrometers*

So far, we have discussed the use of dispersive elements or resonators to separate the different spectral components into individual wavelength channels. Alternatively, the principle of wavelength multiplexing can be utilized to realize on-chip spectrometers. Figure 2(d) sketches the working principle of such a device. Unlike narrowband-resonator-array-based spectrometers, the wavelength multiplexing spectrometer employs broadband filters. The operating principle of the device is therefore distinctively different. Nevertheless, recent work shows that the same principles (discussed below) can be applied to classical dispersive spectrometers[98] and resonator array spectrometers.[101,129] In these cases, the dispersive or resonator elements are effectively treated as broadband filters in order to achieve a higher spectral channel count with a limited number of detectors or to reduce the required quality factor $Q$ of the resonators.

Classical dispersive spectrometers and resonator array spectrometers traditionally operate under the assumption that $G$ is a square, diagonal matrix [Eq. (2)]. In other words, the functions $T_i(\lambda_j)$ are assumed to be zero for all $\lambda_{j\neq i}$. For wavelength multiplexing spectrometers, however, each $T_i(\lambda_j)$ represents a broadband filter transmittance and is composed of a linear combination of many wavelengths. To allow determination of an unknown input spectrum $S(\lambda)$, the matrix $A$ is generally calibrated with a tunable laser (or a known broadband source in conjunction with a calibrated spectrometer). Once the matrix $A$ is known, the wavelength multiplexing spectrometer can be used to measure and reconstruct unknown input spectra based on the methods described in Sec. 3. Wavelength multiplexing spectrometers are thus the first type of spectrometers we encounter that belong to the class of so-called computational spectrometers. Computational spectrometers generally suffer from longer reconstruction times than classical dispersive and resonator-based spectrometers. On the other hand, computational spectrometers are generally more robust against fabrication imperfections, since potential imperfections, such as variations in waveguide thickness throughout the chip, are captured in the calibration of matrix $A$.

The operating bandwidth $\Delta\lambda$ of wavelength multiplexing spectrometers is determined by the wavelength range over which the matrix $A$ is calibrated. For a given $\Delta\lambda$, the resolution $\delta\lambda$ and the spectral channel count $N$ are then dictated by the choice of filters as well as the reconstruction algorithm. Taking advantage of the computational reconstruction and prior knowledge of the spectrum, the number of filters $M$ can be significantly smaller than $N$.[102,105,106] Multiplexing spectrometers thus allow for a reduced device footprint with similar resolution to classical dispersive spectrometers. Increasing the resolution of the device, however, is not as straightforward as just increasing the number of filters. It is important that the functions $T_i(\lambda)$ give a unique response across the operating bandwidth. The uniqueness of an individual filter's response with wavelength is generally quantified with the spectral correlation function:[131]

$$C(d\lambda, i) = \frac{\langle T_i(\lambda) T_i(\lambda + d\lambda)\rangle}{\langle T_i(\lambda)\rangle \langle T_i(\lambda + d\lambda)\rangle} - 1, \tag{7}$$

with $d\lambda$ representing the spacing between wavelength points and where $\langle f(\lambda)\rangle$ represents the averaging of the function $f(\lambda)$ with respect to $\lambda$. When averaged over all filters, the spectral correlation function should peak at $d\lambda = 0$ [Fig. 3(b)]. The half-width at half-maximum (HWHM) can then be used as a proxy for the spectral resolution $\delta\lambda$.[57] Here, we note that one can experimentally achieve a $\delta\lambda$ much smaller than the HWHM of the averaged spectral correlation function[124] when the optical SNR is sufficiently high. Nevertheless, $C$ remains a key figure-of-merit when comparing the spectral resolving power of different spectrometer designs.

The choice of filters determines the scaling behavior of the device. Broadband filter implementations include random scattering,[57,104,132] Mach–Zehnder interferometers (MZIs),[51,133–143] multimode interference,[102,144,145] stratified waveguides,[105]

**Table 1** Overview of Performance Metrics for Representative Examples of Each Spectrometer Type[a]

| Ref. | Category | Method | $\lambda_c$ (nm) | $\delta\lambda$ (nm) | $\Delta\lambda$ (nm) | $F$ (mm$^2$) | $D$ |
|---|---|---|---|---|---|---|---|
| [84] | Classical | Echelle grating | 1550 | 0.5 | 60 | 9 | 121 |
| [86] | | Echelle grating | 1300 | 4.5 | 18 | 0.02 | 4 |
| [87] | | Echelle grating[b] | 1300 | 7 | 1400 | 4 | |
| [89] | | AWG | 1545 | 0.2 | 20 | 64 | 50 |
| [93] | | Cascaded AWGs | 1550 | 1 | 195 | 110 | 195 |
| [95] | | Planar holograms | 740 | 0.15 | 148 | 200 | 926[c] |
| [98] | | Metalenses[d] | 1550 | 0.14 | 50 | 0.01 | 32 |
| [99] | Resonator array | MRR | 1580 | 0.6 | 50 | 1 | 84 |
| [100] | | PhC cavity | 840 | 0.3 | 35 | 0.004 | 100 |
| [101] | | MRR[d] | 809 | 0.17 | 12 | 0.15 | 3 |
| [51] | Multiplexing | FT | 1550 | 0.03 | 0.78 | | 14 |
| [102] | | Multimode spiral | 1520 | 0.01 | 2 | 0.25 | 40 |
| [103] | | Speckle-enhanced FT | 1556 | 0.003 | 12 | 100 | 600[e] |
| [104] | | Scattering | 1556 | 0.25 | 30 | 0.0004 | 8 |
| [105] | | Stratified waveguides | 1560 | 0.45 | 180 | 0.009 | 32 |
| [106] | | Coherent network | 776 | 0.02 | 12 | 0.11 | 8 |
| [107] | | Disordered lattice | 1545 | 0.015 | 40 | 1 | 4096[c] |
| [108] | SWIFTS | Lippmann | 633 | 0.16 | 256 | 0.032 | 2000[f] |
| [109] | | Tunable SWIFTS | 1500 | 40 | 1000 | 0.001 | 5 |
| [110] | | Multi-aperture Lippmann | 842.5 | 0.2 | 75 | 5.12 | 160 |
| [111] | Tunable narrowband | MRR | 1580 | 0.15 | 19 | 0.6 | 1 |
| [112] | | PhC cavity | 1455 | 0.5 | 12.3 | | 1 |
| [113] | | FP cavity array | 1472 | 0.43 | 73.2 | 0.026 | 5 |
| [114] | | MRR + MRR array | 1550 | 0.005 | 9.7 | 0.35 | 11 |
| [115] | | Photonic molecule[d] | 1550 | 0.04 | 100 | 0.004 | 1 |
| [116] | | Microdisk[d] | 1505 | 0.01 | 0.3 | 0.24 | 1 |
| [117] | | Cascaded MRRs[d] | 1550 | 0.1 | 200 | 0.004 | 3 |
| [118] | | Cascaded MRRs[d] | 1440 | 0.008 | 520 | 0.6 | 1 |
| [52] | FT | dFT[g] | 1560 | 0.2 | 20 | 1.9 | 1 |
| [119] | | Thermo-optic | 1550 | 0.9 | 56 | 0.9 | 1 |
| [120] | | MRR assisted TO | 1571 | 0.47 | 90 | | 1 |
| [121] | | MEMS | 1550 | 0.2 | 100 | 0.075 | 1 |
| [122] | | 2D FT | 1550 | 0.125 | 200 | | 128 |
| [123] | Tunable broadband | Multimode spiral | 1554 | 0.015 | 2 | 3.36 | 12 |
| [124] | | Cascaded MZIs | 1510 | 0.01 | 200 | 8 | 1 |
| [125] | | Cavity-enhanced mode mixing | 1550 | 0.005 | 100 | 1.5 | 1 |

[a]For each example, the spectrometer category, implementation method, center wavelength $\lambda_c$, spectral resolution $\delta\lambda$, bandwidth $\Delta\lambda$, footprint $F$, and number of detectors $D$ are listed. A more complete overview can be found in Appendix A.
[b]Requires cryogenic temperatures and NbN superconducting nanowires for single-photon detection.
[c]Makes use of an off-chip camera.
[d]Employs computational spectral reconstruction based on a calibrated $A$ matrix.
[e]Each data point consists of an average over a column of off-chip camera pixels.
[f]Number of metal scattering centers.
[g]Digital Fourier transform (dFT).

coherent networks,[106,146] self-coupled waveguides,[147] disordered MRR lattices,[107] and disordered in-plane metasurfaces.[148] For a straightforward filter-array approach,[105,147] linear scaling of the footprint with the number of measurement channels $M$ holds. As a result, either the resolution or bandwidth will scale linearly with the filter array footprint. For other approaches, the spectral correlation of the filter transmittance depends on the OPL.

Spatial heterodyne or stationary Fourier-transform (FT) spectrometers [Fig. 2(e)][51,133–143] consist of an array of MZIs with a unique OPD. In the case that $N = M$ with linearly spaced OPDs, the inversion of matrix $G$ becomes equivalent to a classical Fourier transform,[133,134] hence the name FT spectrometer. The resolution of such a spectrometer is dictated by the FSR of the MZIs. This FSR scales inversely proportional with the OPD of the MZI. A long path length will give a small FSR and thus allow for a high spectral resolution. Additionally, stationary FT spectrometers again follow a linear scaling law. For high spectral resolution a large number $M$ of interferometers is needed, which again results in a trade-off between footprint and $\delta\lambda$.

For random-scattering-based spectrometers, due to the occurrence of multiple scattering events, the effective path length on-chip can be much longer than the length of the scattering region. As a result, the resolution no longer improves linearly with the geometric dimension of the device. Instead, in the diffuse regime, a quadratic scaling is observed.[57] Similarly, evanescent coupling between waveguides in a spiral[102] or coupling to MRRs[106,107,146] can be employed to increase the OPL and thus modify the scaling behavior of the spectrometer.

Alternatively, cascading broadband filter elements, such as disordered metasurfaces,[148] can achieve a more narrowly peaked spectral correlation function. In this case, the performance metrics of the device are still expected to scale linearly with the number of filter elements.

### 4.4 Stationary-Wave Integrated Fourier-Transform Spectrometers

The last type of spectrometer we discuss in the category of spatially dispersed spectrometers is the stationary-wave integrated Fourier-transform spectrometer or SWIFTS, which can also be considered a special class of wavelength multiplexing spectrometers. The SWIFTS operates by creating a standing-wave interference pattern in the waveguide [Fig. 2(f)]. By integrating a linear array of detectors, the spatial intensity distribution of the standing wave can be mapped. From this intensity distribution, the input spectrum can be inferred. Similar to the spatial heterodyne FT spectrometers, spectral reconstruction based on a standing-wave interferogram sampled at constant pitch is equivalent to a classical Fourier-transform.

We distinguish three SWIFTS configurations: the Lippmann configuration,[108,110] the counterpropagative configuration,[149] and the copropagative configuration.[150] In the Lippmann configuration, the standing wave is created by means of a reflector, such that the reflected light interferes with the incident light. In the counterpropagative configuration, light is propagating in both directions of the spectrometer waveguide. In the configuration, two parallel waveguides with different effective indices are used to generate a standing-wave interference pattern in between the two waveguides.

Regardless of the configuration, the resolution of an SWIFTS is limited by the length of the interferogram. Again, a linear relation emerges where the resolution improves with increasing device length. The bandwidth at a given device length depends on the sampling rate, i.e., the spacing between the detectors $\Delta x$.[151] Given the relatively large footprint of currently available integrated photodetectors,[152] demonstrated SWIFTSs employ scattering arrays in combination with off-chip detector arrays to achieve a narrower on-chip sampling pitch. As a result, $\Delta x$ and consequently $\Delta\lambda$ are diffraction-limited.

One method to increase $\Delta\lambda$ is to couple the input spectrum into multiple waveguides[110] or a slab waveguide[108] (Table 1). This allows the detectors/scattering centers to be spread out laterally, enabling an enhanced sampling rate along the standing-wave pattern. Additionally, the coupling of the input light into multiple waveguides [Fig. 2(e)] or a slab waveguide allows for an increased spectrometer etendue, a topic we explore further in Sec. 6.

As an alternative approach, one can improve $\Delta\lambda$ by applying a phase shift to the input light, e.g., with a tunable MZI,[151] electro-optic modulators,[109,153] or thermo-optic modulators.[154] By implementing a phase delay between the two inputs (in a counterpropagative configuration), one is able to shift the location of the center of the interferogram. By stepwise increasing the phase delay and consecutive sampling of the interferogram, the entire interferogram can be sampled even at a large detector pitch. Note that this measurement technique requires active tuning of the spectrometer, and we have effectively changed the spatially dispersed SWIFTS into a combined spatially dispersed and time-domain modulated device. The matrix $G$ now must incorporate the transmission functions for every wavelength in both space and time.

## 5 On-Chip Spectrometers Based on Time-Domain Modulation

We have discussed spatially dispersed on-chip spectrometers in the previous section. In the final paragraph, we encountered an example of a spectrometer that utilizes time-domain modulation. In this section, we explore other on-chip spectrometers based on time-domain modulation. Instead of spatially spread static filters (Fig. 1), tunable filters are used in time-domain modulated spectrometers. This allows for modulation of the filter's spectral response as a function of time. As a result, instead of a detector array, only a single detector is required. Now the photodetector readout $y$ gives a time sequence of intensity readings from the single detector, instead of the signal readout of the detector array. Each element $y_i$ thus gives the readout at one particular point in time or, in other words, at one specific state of the tunable filter. Each row in the matrix $G$ now corresponds to a filter transmittance function $T_i(\lambda)$ for one particular tunable filter state $i$.

### 5.1 Narrowband Tunable Filter Spectrometers

The first variant of such a time-domain modulated spectrometer we discuss is a spectrometer based on a narrowband tunable filter.[111–113,115,116,118,155,156] A common choice of narrowband filter is an MRR or microdisk resonator integrated with an optical phase modulator, such as a thermo-optic phase shifter [Fig. 4(a)].[111,116,156] Other filter choices include Fabry–Pérot (FP)[112,113] and PhC cavities.[155]

Tunable-filter-based spectrometers tend to have an advantage over resonator arrays in terms of optical crosstalk. The advantage arises from the fact that only a single resonator is used.

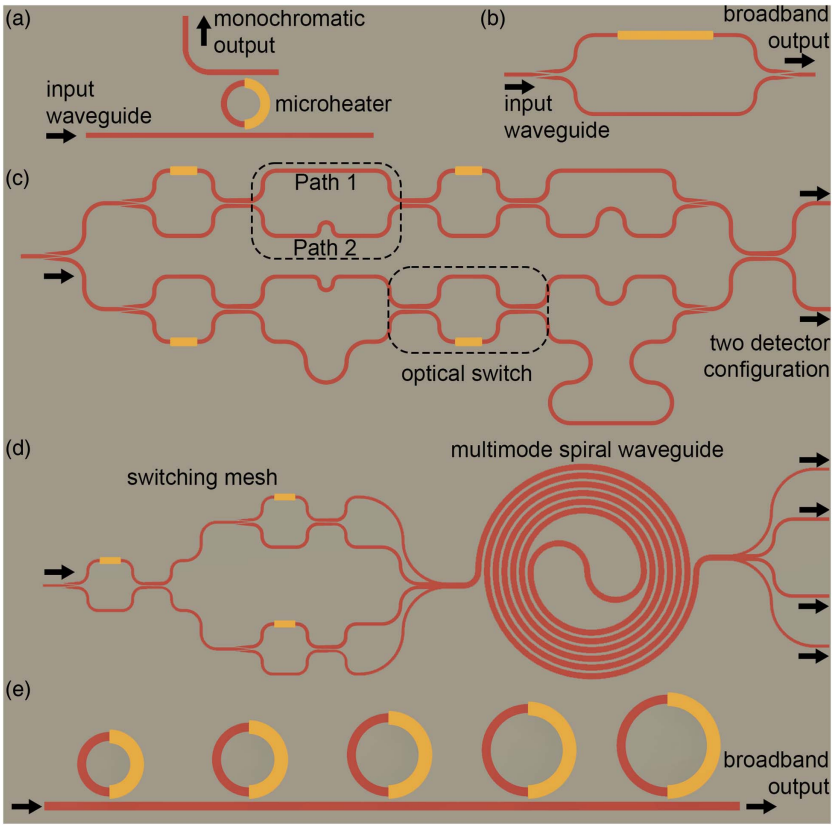


**Fig. 4** Schematic representations of the types of time-domain modulated spectrometers. (a) Narrowband filter spectrometer based on an MRR with a thermo-optic phase shifter. (b) FT spectrometer consisting of an MZI with a tunable delay in one of the arms. (c) dFT spectrometer architecture[52] with double detector configuration. In each arm of the main MZI, optical switches route the light to one of two possible paths (either path 1 or path 2). Each combination of switch states gives a unique OPD at the main MZI output. (d) Tunable broadband filter spectrometer, where a wavelength multiplexing spectrometer based on an evanescently coupled multimode spiral waveguide is combined with an optical switching matrix.[123] (e) Cascaded tunable MRR spectrometer.[118]

Consequently, we do not have to worry as much about fabrication imperfection and the resulting resonator-to-resonator variation.

Similar to resonator array spectrometers (Sec. 4.2), the operating bandwidth of a tunable narrowband filter is limited by the FSR of the resonator. In addition to the FSR, the attainable wavelength tuning range can limit $\Delta\lambda$. The resolution is again not directly limited by the physical size. Instead, $\delta\lambda$ is determined by the quality factor $Q$. Since only a single narrowband filter and photodetector are required, the footprint of the spectrometer can be much smaller than that of spatially dispersed spectrometers (Table 1). Furthermore, we have a unique scaling behavior, where both $N$ and $\delta\lambda$ do not scale with the device footprint, but instead depend on the resonator's $Q$ and the phase modulation range.

In the case of a tunable MRR,[111] we again have that reducing the ring radius leads to an increasing FSR, but decreasing $Q$ when radiative bending loss takes over. Hence, a similar trade-off between resolution and bandwidth arises as for MRR arrays. FP and PhC cavities, on the other hand, can exhibit high $Q$ with a large FSR. These large FSR cavities, however, generally still exhibit a limited $\Delta\lambda$, due to a limited tuning range.

There again exist several approaches to achieving both a broad bandwidth and a high resolution. First, the operating bandwidth can be extended by cascading multiple tunable cavities,[113,155] in which the wavelength tuning range of each is centered around a different part of the total bandwidth, or by co-integration of a resonator with a tunable lattice filter[157,158] or tunable FT spectrometer (Sec. 5.2).[120] A third approach entails co-integration of a tunable narrowband filter with a dispersive element.[114,159–162] Such a co-integrated design is similar to cascaded dispersive spectrometers (Sec. 4.1). The dispersive element is used to split the broadband signal into multiple wavelength bands. Each output of the dispersive element is now routed to a tunable filter (instead of a second dispersive element), where we perform a high-resolution scan of the wavelength band. Alternatively, the order of co-integrated components can be reversed.[120,159,161,162] In that case, the broadband signal first passes a resonator, where a set of wavelengths with a spacing equal to the FSR is filtered out of the input. The filtered wavelengths are then sent through a coarse dispersive

splitting element, which routes each of the filtered wavelengths to a specific detector. Both the cascaded cavity as well as the co-integrated approaches, however, require multiple photodetectors as well as an increased device footprint. The final approach we discuss is the engineering of the MRR system to obtain operation spanning multiple FSRs. A broadened $\Delta\lambda$ could, for example, be obtained by the Vernier effect[163,164] or using microgear resonators.[165] Recent works employ dispersion engineering in photonic molecules,[115] selective mode coupling,[166] or cascaded MRRs.[117,118] Note that in these cases, the narrowband filter is effectively converted into a (sparse) broadband filter (Sec. 5.3) and reconstruction of the input spectrum is based on a measured matrix $A$ (Sec. 3).

### 5.2 Fourier-Transform Spectrometers

The second type of spectrometers based on time-domain modulation is the FT spectrometer [Fig. 4(b)], which can be regarded as the time-domain modulated counterpart of the stationary FT spectrometer that we discussed in Sec. 4.3. An FT spectrometer consists of a variable MZI, where in one or both of the arms a tunable delay is integrated to generate a tunable OPD between the two arms. The tunable delay can be implemented in various ways, including electro-optic modulators,[167,168] thermo-optic modulators,[119,120,169–171] or MEMS.[121,172] The resolution is inversely proportional to the maximum OPD that can be achieved by the tunable delay. As a result, for a given choice of modulator, we again observe a linear scaling behavior, where the resolution improves with increasing device footprint.

To increase the OPD beyond the typical on-chip phase modulators' tuning range, a combination of spatial heterodyne and time-domain modulated FT can be used.[170,172,173] In this case, each MZI is used to tune the OPL over a unique range of OPDs. A different combination of spatial heterodyne and time-domain modulated FT can be implemented by cascading a tunable FT with a spatial heterodyne FT spectrometer.[122] An alternative device architecture, the on-chip digital FT (dFT) spectrometer [Fig. 4(c)],[11,52,171,174–178] has also been proposed. In a dFT spectrometer, we integrate a cascaded array of optical switches on each arm of the interferometer. Each switch allows for toggling the optical path between two waveguides. Each permutation of the optical switch states results in a unique OPD. Since switching of waveguide paths presents a far more efficient way to introduce phase delay compared to electro-optic or thermo-optic modulation, the waveguide lengths needed in dFT spectrometers to achieve the same OPD can be more than two orders of magnitude shorter. Instead of a linear scaling with footprint, the number of optical states $M$ is proportional to $2^k$, where $k$ is the total number of optical switches. As a result, the spectral resolution also scales with $2^k$. This exponential scaling allows for a compact integrated device with a high optical performance. It is worth highlighting that the dFT spectrometer represents the first example of a more generic class of time-domain modulated spectrometers based on cascaded tunable elements to achieve exponential scaling, where the total number $M$ of optical states scales with the product of state numbers across all elements. We shall see more examples of this class of spectrometers in other sections.[118,124,125,179]

Finally, we note that for both stationary as well as time-domain modulated FT spectrometers in a single-detector configuration, on average, half of the photons in a broadband signal will be tossed out, since only constructively interfering photons are retained. These "lost" photons can be reclaimed by implementing a two-detector configuration. In this two-detector configuration, instead of a $2 \times 1$ combiner at the end of the MZI, a $2 \times 2$ coupler is used [Fig. 4(c)]. By doing so, we can actually double the signal. If the spectrometer noise is dominated by the detector noise,[180] the two detector approach achieves a net gain of the SNR by a factor of $\sqrt{2}$ compared to the single-detector configuration.

### 5.3 Tunable Broadband Filter Spectrometers

In this class of spectrometers, a broadband transmission spectrum is tuned. These spectrometers employ the same principles as wavelength multiplexing spectrometers (Sec. 4.3), with the addition of active modulation of the broadband filters to vary the signal at one[124,125,181] or multiple photodetectors.[123,179,182–184]

Similar to the dFT spectrometer, a photonic-switching-based approach has been applied to multimode-interference-based wavelength multiplexing spectrometers [Fig. 4(d)].[123,179,182] Here, the switches are used to selectively launch modes into a multimode waveguide. Since the effective OPL in the multimode waveguide is independent of the optical switches, the spectral resolution does not directly depend on the number of optical switches $k$. Instead, $M$ and $\Delta\lambda$ change with the number of optical switches. The relation between $M$ and $k$ depends on the exact device implementation. Scaling with $k$,[123] $2^k$,[179] and $k^2$[182] has been demonstrated.

Alternative tunable broadband filter implementations include tunable coherent networks,[181,183] tunable-cavity-enhanced mode mixing,[125] and disordered metalenses with beam steering.[184] Similar to their stationary counterparts, these approaches employ resonators, evanescent coupling between waveguides, and cascaded filter elements to increase the effective OPL and decrease the correlation of transmission functions $T_i(\lambda)$ [Eq. (7)]. As a result, a complicated scaling behavior is recovered. In the case of cavity-enhanced mode mixing, for example, the resolution is found to be relatively independent of the overall size of the resonator, but instead scales approximately linearly with the size of the mode mixing region.[125]

Finally, another tunable-MZI-based spectrometer was recently proposed.[124] Instead of an FT spectrometer with a single MZI, multiple cascaded MZIs were used to generate a complicated interference signal at the output. As a result, the resolution is no longer limited by the maximum OPD that can be achieved in a single MZI. An exponential scaling is recovered, where the scaling depends on the number of cascaded elements $k$ and the number of states per element. An alternative approach to this type of exponential scaling employs cascaded MRRs [Fig. 4(e)],[118] which can be used to implement a broadband tunable filter (Sec. 5.1). With four tuning states per ring, $M$ is proportional to $4^k$. With a dispersion-engineered six-ring design ($M = 4096$) a record-high resolution-to-bandwidth ratio was achieved (Table 1).

## 6 Constraints to On-Chip Spectrometer Implementation

Now that we discussed the different types of PIC-based spectrometers and their performance metrics, we proceed to assess some fundamental constraints and design considerations for on-chip spectrometers. These constraints determine the applicability of on-chip spectrometers under different circumstances.

In the following section, we treat the application areas where PIC-based spectrometers promise a significant impact.

The most significant limitation of waveguide-based spectrometers is the optical throughput: compared to free-space spectrometers, PIC-based spectrometers generally exhibit significantly reduced optical throughput due to the small etendue of on-chip waveguides. In some spectrometer designs, such as resonator array spectrometers,[100] SWIFTS,[108] and specific wavelength multiplexing spectrometers,[103,106,139,140,146] the spectrometer etendue can be increased by coupling into multiple waveguides or slab waveguides. Nonetheless, the etendue generally remains small compared to free-space spectrometers, such as 2D filter-detector array spectrometers.[185,186] Therefore, PIC-based spectrometers work best with light sources that have a high degree of spatial coherence. When dealing with a large-area light source with low spatial coherence, the performance of on-chip spectrometers is severely limited.

Another important consideration relating to spectrometer applicability is the material platform on which to implement the spectrometer. Firstly, the wavelength range covered by PIC spectrometers is limited by the material platform. Silicon-on-insulator (SOI), which, due to its compatibility with standard complementary metal-oxide-semiconductor (CMOS) processing, allows for low-cost and scalable manufacturing, is the most widely used platform for PICs in the near-infrared (near-IR). However, due to considerable absorption in the visible range and at longer mid-IR wavelengths (>3.5 μm for oxide-cladded devices and >6.7 μm for suspended Si waveguides), the SOI platform is not suited for spectrometry outside of the short-wavelength part of the IR spectrum. In the visible range, silicon nitride (SiN) has emerged as a CMOS-compatible alternative.[8,187] Other material platforms are required for spectroscopic sensing in the so-called "fingerprint region" (7–20 μm, containing the primary absorption bands of many chemical and biological molecules).[7,188]

Beyond the transparency window, the choice of material can influence spectrometer performance. Waveguide losses are generally dominated by scattering loss, due to sidewall roughness.[10] Processing capabilities and the resulting sidewall roughness are related to the choice of material platform. In the near-IR, SiN has emerged as a low sidewall roughness and thus ultralow-loss waveguide platform.[8,10] Lower waveguide losses not only promise higher optical throughput, but can directly influence spectrometer performance metrics. For example, due to these ultralow losses, the SiN platform promises higher $Q$ resonators[189] than SOI, allowing for higher resolution in resonator-based spectrometers. Because of the lower refractive index contrast with the oxide cladding, however, SiN waveguides exhibit larger bending losses than Si waveguides. Consequently, SiN waveguides require larger bending radii, resulting in a larger device footprint and limited microring FSR.

Finally, we discuss the thermal stability of on-chip spectrometers. Changes to the on-chip temperature generate refractive index changes in the waveguide through the thermo-optic effect. As the TO coefficient in most PIC platforms is positive, an increase in temperature generally yields redshifted transmittance functions $T_i(\lambda)$.[124,147,190–192] The most straightforward solution is active monitoring and regulation of the temperature of the PIC, e.g., with a thermo-electric cooler. Such thermal control, however, increases the power consumption of the device.

Alternatively, monitoring the on-chip temperature allows for compensation for temperature variations by applying a correction to the matrix $G$ that accounts for the thermally induced shift in $T_i(\lambda)$.[192,193] Consider the case of a classical dispersive or resonator-based spectrometer with a square, diagonal $G$ as a concrete example. At higher temperatures than designed for, wavelength $\lambda_j$ can be collected at detector channel $i < j$ instead of the intended channel $i = j$. When the chip temperature at the time of measurement is known, this offset between the detector and the wavelength channel can be corrected. A drawback in this case of a diagonal $G$ matrix (especially for designs with a larger FSR than $\Delta\lambda$) is potential loss of spectral information,[147] resulting from the fact that the signal at the edge of the bandwidth is no longer collected at any detector. Spectrometer designs based on non-diagonal $G$ matrices, i.e., spectrometers implementing broadband filters, are better equipped to handle large temperature changes, since even though $T_i(\lambda)$ changes with temperature, light from all wavelengths continues to reach the detector. By performing calibration over a large range of temperatures, the entire input spectrum can thus be recovered over a larger temperature range.[147,193]

Finally, thermal stability can be taken into account during the design of the spectrometer.[142] Firstly, the material platform in which the spectrometer is integrated is important. The TO coefficient for SiN, e.g., is significantly smaller than the TO coefficient for Si. Consequently, spectrometers implemented on SiN are generally more thermally stable than on SOI. Secondly, one can aim to design the spectrometer such that the spectral response does not change with temperature, e.g., by adding an extra optical component that compensates for the temperature dependence of the filters.[190,194] In a recent work, an athermal echelle grating[194] was implemented by compensating for the thermally induced tilt in the phase front in the grating with the thermal response of an asymmetric MZI at the input of the device.

## 7 Integrated Photonic Spectrometer Applications

We discuss four application areas where PICs promise key advantages and opportunities as a result of their reduced SWaP-C metrics.

### *7.1 Biological and Chemical Sensing*

Both absorption and Raman spectroscopy are powerful techniques to directly identify chemical and biological samples.[1,14] Due to the size and cost of traditional spectrometers, this spectroscopic analysis is historically performed in a laboratory setting. There is however an increasing demand for spectrometers that can be brought out into the field, enabling on-site analysis for a wide range of applications, including industrial, environmental, or toxic gas sensing,[195] point-of-care diagnostics,[196] bioprocess monitoring,[197,198] and forensics.[199]

Integrated photonics provides a unique opportunity for so-called lab-on-chip system integration, wherein the light source, sensing element, and detector are all integrated into the same platform [Fig. 5(a)].[200–203] Spiral waveguides and on-chip resonators allow for long interaction lengths with a small footprint.[204,205] Compared to other (on-chip) sensing techniques, such as refractive index sensing [Fig. 5(b)],[200] spectroscopic sensing [Fig. 5(c)] offers high selectivity without the need for target-specific functionalization or labeling. Unlike sensors relying on surface functionalization coatings, which are typically for single-use only due to the irreversible binding nature

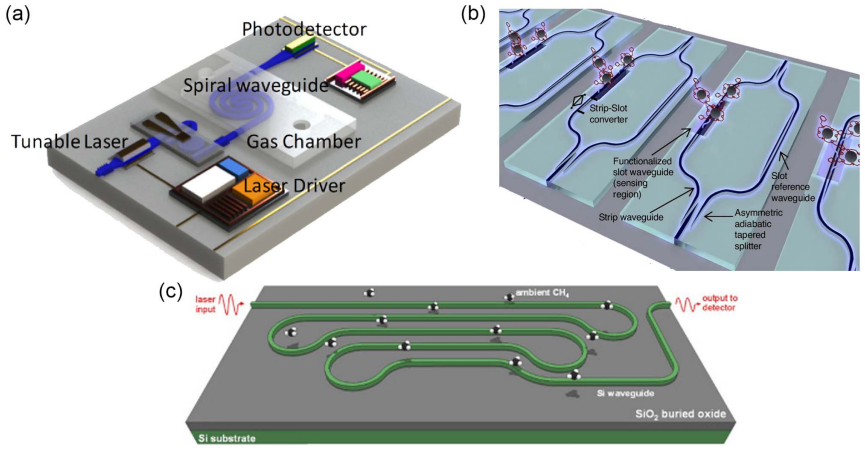


**Fig. 5** (a) Example of an integrated photonic lab-on-chip system. Reprinted with permission from Ref. 210 © Chinese Laser Press. (b) Refractive index sensing for lead detection using functionalized MZIs. Adapted from Ref. 211 under Creative Commons license.[212] (c) Waveguide-based methane absorption sensor. Reprinted with permission from Ref. 213 © Optical Society of America.

of the coatings, lab-on-chip systems based on spectroscopic sensing can be repeatedly used, e.g., for applications where continuous monitoring is needed. Furthermore, waveguide-based sensing can provide enhanced sensitivity in Raman spectroscopy.[206–209]

Recent work in integrated spectrometers for sensing applications includes gas sensing,[162,172] sensing of volatile organic compounds,[128] absorption sensing,[118,138] and Raman spectroscopy.[110] One specific example focused on a spectrometer for sensing multiple gases, such as HF, CO, $H_2S$, and $CO_2$, at wavelengths between 1310 and 1930 nm.[162] The proposed design consisted of a multimode-waveguide-grating-based filter array in combination with tunable MRRs. The authors were able to implement a chip-scale spectrometer for high-resolution sensing (0.08–0.37 nm) over this broad bandwidth using four multimode waveguide gratings as bandpass filters, each centered on a narrow wavelength band of interest (6–10 nm at 1310, 1560, 1570, and 1930 nm). In another study,[118] a cascaded MRR spectrometer is used to measure the reflectance spectra of various plastic and coffee samples as well as the concentration-dependent transmission spectra of various solutions (such as ethanol or glucose aqueous solutions). The authors train a support vector machine to identify the different plastic or coffee samples on the reconstructed spectra. Additionally, the integrated spectrometer achieves a detection limit of 0.1% glucose in solution, comparable to that of a benchtop dispersive and a benchtop FT spectrometer.

### *7.2 Telecommunications*

Optical fibers provide high-bandwidth, low-loss optical communications worldwide. Recent years, however, have seen a significant increase in data traffic and a demand for even faster (6G) data transmission, due to the rise of big data, artificial intelligence, and the internet of things. To keep up with these increasing demands, network communication is being extended from the C+L-bands into the S-, E-, O-, and U-bands. Dynamic control is essential for energy-efficient operation of a multi-band network, allowing for scaling up or scaling down the network depending on the network traffic.[214–216]

Dynamic (software-based) control of modern networks (Fig. 6) is only possible with optical network monitoring.[217,218] Efficient monitoring throughout the entire network requires low-cost, compact monitors that are able to track the individual wavelength channels. Integrated photonic spectrometers have the potential to fulfill these requirements for low-cost large-scale manufacturing and can provide real-time monitoring of the individual channels. Initial proposals for such optical channel monitors rely on classical dispersive elements such as echelle gratings[219] and AWGs[220] to directly monitor the optical power, SNR, and wavelength drift in the channels. An alternative monitoring approach is so-called "homodyne detection", for which monitoring is based on the interference spectrum between the monitored signal and a tunable laser.[214,221] In a recent work,[222] a spectrometer design using a tunable MRR cascaded with two interlaced AWGs was proposed for high-resolution (~1.4 GHz or ~0.01 nm) optical network monitoring in the C-band (1530–1565 nm) on a SiN platform.

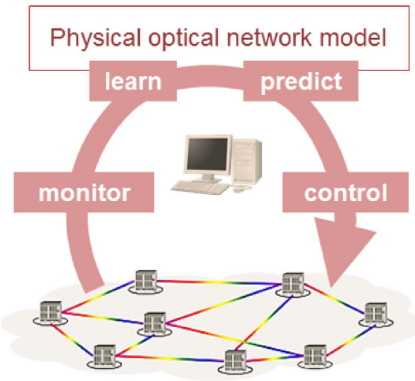


**Fig. 6** Dynamic software-based control and management of optical networks. Reprinted with permission from Ref. [223] © Optical Society of America.

### 7.3 Spectral Domain Optical Coherence Tomography

Optical coherence tomography (OCT) is an interferometric 3D imaging technique that provides high-resolution, cross-sectional imaging for a wide range of scientific and medical applications.[224] It is the gold standard for retinal imaging (Fig. 7) in ophthalmology and is increasingly used in cardiology, dermatology, and other medical fields. Additionally, OCT is applied in non-destructive testing (NDT) to provide information on subsurface structures and uniformity in manufacturing, aviation, automotive, display panels, and medical devices.

While there are a few embodiments of time-domain and Fourier-domain OCT, spectrometers play a crucial role in spectral-domain optical coherence tomography (SD-OCT). The bandwidth and resolution of the spectrometer directly influence the axial resolution and signal-to-noise ratio of the OCT system, making it an essential component in the performance of OCT. Traditionally, benchtop dispersive spectrometers are used in OCT systems, but there have been recent investigations into integrated photonic approaches. PICs allow for the miniaturization of OCT systems, making them more portable and accessible for various applications, including point-of-care diagnostics and field use. Additionally, the integration of photonic components onto a single chip can lead to substantial cost reductions by simplifying manufacturing processes and reducing the need for bulky, discrete optical elements. In recent years, there has been an effort to bring other components of the OCT system onto PICs,[226] including beam splitters,[227,228] delay lines,[227,229] and light sources.[230]

Notably, one of the latest works in the field developed two OCT spectrometer designs based on AWGs on a SiN platform. The devices featured sufficiently broad bandwidths (22 and 48 nm centered around 800 nm) to provide high axial resolution (10.7 and 6.5 μm, respectively).[225] These were the first instances where PIC-based spectrometers were used to provide *in-vivo* retinal OCT imaging (Fig. 7) and achieved sensitivity above 90 dB. High sensitivity is crucial for medical applications due to the critical importance of accurate diagnosis, as it ensures detailed and precise imaging necessary for identifying and monitoring medical conditions. This innovation builds on AWG-based spectrometers[92,126,231] and OCT demonstrations,[161,232,233] which focus on wavelengths around 800 or 1300 nm, including imaging demonstrations of human skin.[228] In a follow-up work,[234] an OCT spectrometer comprised of a single, 512 channel AWG was used for *in-vivo* imaging of zebrafish, larvae, and human skin with a sensitivity of 92 dB.

### 7.4 Astronomy

Spectroscopic techniques are fundamental to astronomy and are used to determine chemical composition, measure motion, and detect exoplanets, among other applications.[235,236] These astrophysical studies require large-diameter ($D$) telescopes to collect light from faint and distant sources. Conventional spectroscopic instrumentation scales in size with $D$ and consequently scales with $D^2$ to $D^3$ in terms of volume, mass, and cost.[235,237] The field of astrophotonics provides a path towards spectroscopic instrumentation at reduced SWaP-C.

In astrophotonics, light is coupled from a (large) telescope into a fiber and can then be coupled further into an integrated circuit. Although light coupling from the telescope into a fiber was already proposed in 1988,[238] the coupling efficiency has been limited by atmospheric turbulence.[236] With recent developments in adaptive optics, the coupling efficiency to fibers has significantly improved,[239] and astrophotonics is becoming increasingly important to astronomical instrumentation. For a more complete overview of the field of astrophotonics, we direct interested readers to other review articles.[236,240] Here, we briefly discuss integrated photonic spectrometers developed for astronomical purposes.

Although there is interest in using echelle gratings (due to their larger finesse)[235,237] or FT spectrometers (for high-resolution, broadband operation),[235] most demonstrations of integrated spectrometers for astronomy have so far focused on AWGs (Fig. 8).[91,237,241] One notable study[242] found that by removing the input waveguides and instead coupling light directly from a fiber into the free propagation region of an AWG, the resolution increased ($\delta\lambda$ reduced from 0.63 to 0.22 nm at 1540 nm wavelength) while simultaneously allowing for light injection from multiple fibers or sources into the same spectrometer. Similarly, on the output side of the AWG, the different spectral channels were not collected in a set of output waveguides. Instead, for these astronomical spectrometers, the focal plane of the output coupler was aligned with the edge of the chip, and the spectrum was imaged with an off-chip camera.[91,242] In another recent study,[144] the solar spectrum was collected with a telescope and routed to a multimode interference spectrometer. The authors showed accurate reconstruction of the Fraunhofer A absorption line in the solar spectrum (located at a wavelength of 760 nm).

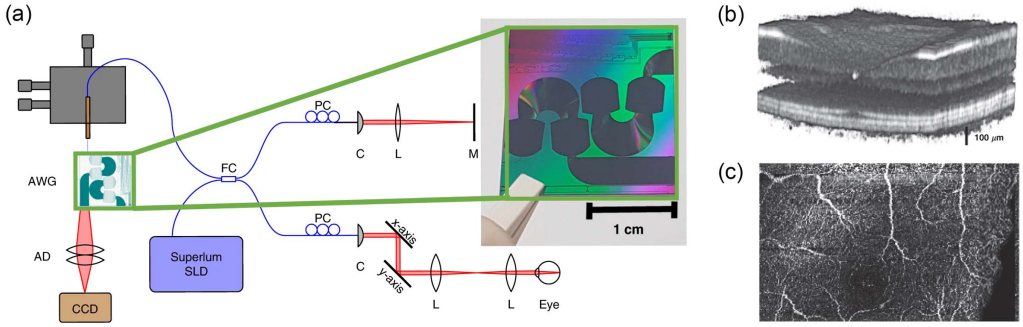


**Fig. 7** (a) OCT set-up for retinal imaging with an AWG-based dispersive spectrometer. (b) 3D image of the retina as recorded with this set-up. (c) Corresponding OCT angiography (OCTA) image calculated from B-scan repetitions. Adapted from Ref. 225 under Creative Commons license.[212]

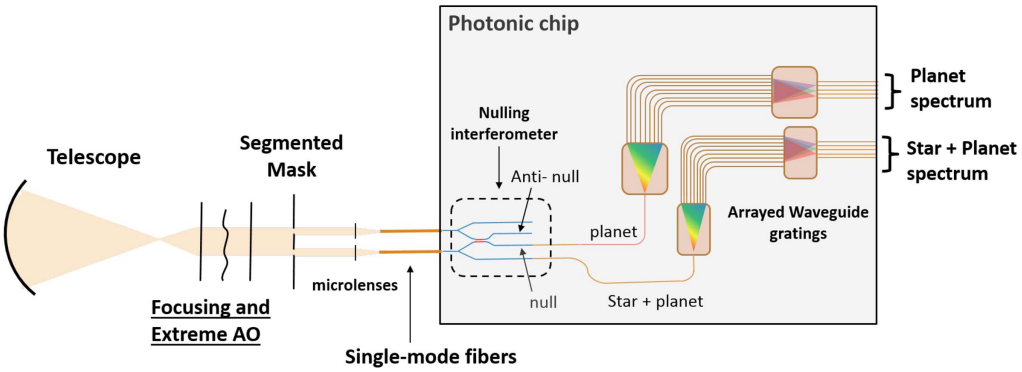


**Fig. 8** Schematic of a telescope set-up integrated with AWG-based on-chip spectrometers for exoplanet spectroscopy. Reprinted from Ref. [235] under Creative Commons license.

## 8 Selecting the Right Spectrometer

In this section, we discuss how to select the right spectrometer for an intended application. Per application, the ideal spectrometer type depends on the requirements with respect to the performance metrics ($\delta\lambda$, $\Delta\lambda$, and SNR). Here, we start with the spectrometer of choice when resolution is the most important metric. In Secs. 4 and 5, we discussed the relationship between resolution and footprint for the different types of spectrometer designs [Fig. 9(a)]. In this section, we focus on whether the intended application requires narrowband or broadband operation [Fig. 9(b)].

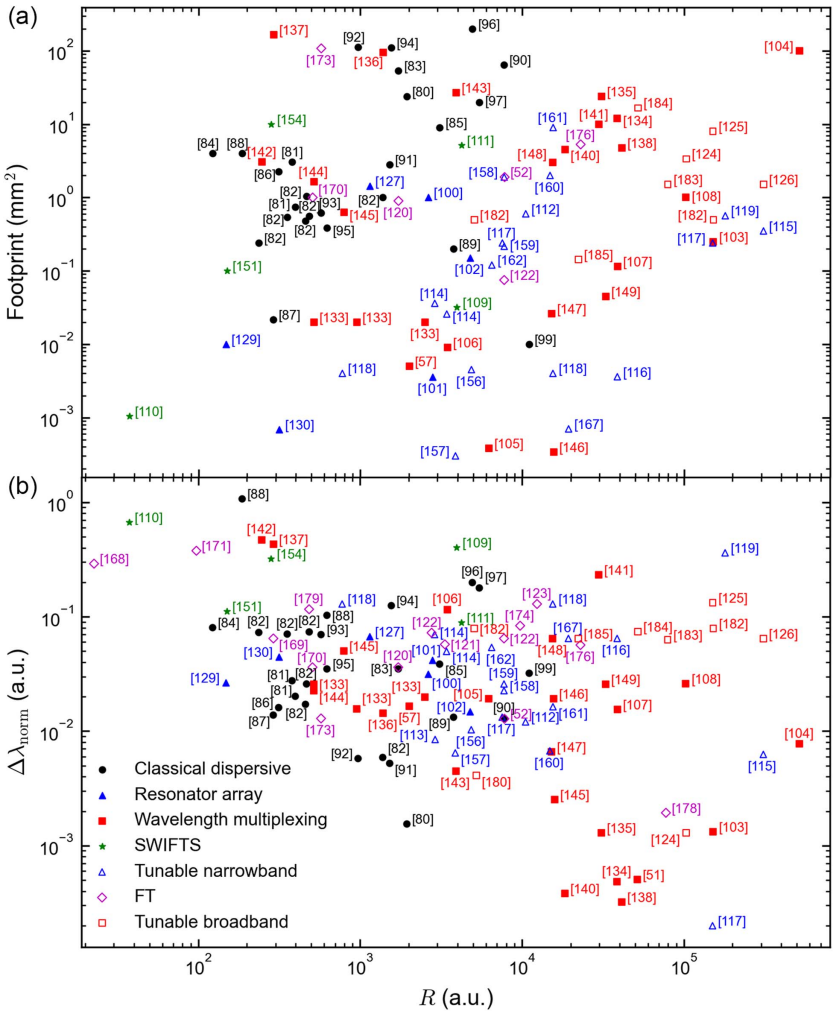


**Fig. 9** Here we plot (a) the spectrometer footprint and (b) the normalized bandwidth ($\Delta\lambda_{\text{norm}} = \frac{\Delta\lambda}{\lambda}$) as a function of the resolving power ($R = \frac{\lambda}{\delta\lambda}$) for various integrated spectrometers. An overview of the plotted data can be found in Appendix A.

For narrowband operation, resonator-based spectrometers are promising candidates. Resonator-based spectrometers allow for very high resolution that is only limited by the resonators' $Q$. Additionally, due to the narrow transmission function of a resonator, these spectrometers are able to selectively measure the target wavelengths without interference from any of the background. Notably, in recent work, a tunable MRR in combination with an MRR array was used to achieve a high resolution of 5 pm over a bandwidth of 9.7 nm.[114] Alternatively, spatially dispersed wavelength multiplexing spectrometers, such as stationary FT[51] or multimode-interference-based spectrometers,[102] are well-suited for high resolution under narrowband operation. With a so-called speckle-enhanced FT spectrometer,[103] a high resolution of 3 pm over a 12 nm bandwidth was achieved (Table 1). However, we do note that this speckle-enhanced FT relies on the detection of light propagating both in strip waveguides as well as the substrate of the SOI PIC. Therefore, an off-chip camera is required to detect the spectrometer's output signals.

For broadband operation, due to the bandwidth-resolution trade-off, resonator-based spectrometers generally are not the best choice. Instead, a design that allows for exponential scaling with device footprint is needed to achieve high-resolution, broadband operation on-chip. Designs that allow for such scaling include cascaded MRRs,[118] dFT, and tunable broadband filter spectrometers.[124] The unique scaling in these types of spectrometers is ideal for achieving a large number of optical states $M$, thus enabling enhanced broadband performance. Furthermore, we note that these spectrometers' bandwidth is actually not limited by the bandwidth of the individual components, such as the optical switches. A switching-based device, for example, does not require perfect power switching between the different waveguides, as long as each switch permutation generates a unique spectral transmittance $T_i(\lambda)$. Ultimately the bandwidth and resolution of these spectrometers will only be limited by the waveguide single-mode condition and the SNR.

In the remainder of this section, we discuss the best choices for integrated spectrometers based on the SNR. Time-domain FT and tunable broadband filter spectrometers exhibit a theoretical SNR advantage over spatially dispersed and time-domain modulated narrowband filter spectrometers, known as the "multiplex advantage" or "Fellgett's advantage".[243] This SNR advantage occurs when the main source of noise is from the photodetector (as opposed to light-intensity-dependent noise contributions, such as photon shot noise or background noise).[180] For classical dispersive and resonator-based spectrometers, the input spectrum is split into many spectral channels and each spectral channel is detected separately. Multiplexing spectrometers and SWIFTS similarly spread the optical intensity over multiple detectors. As a result, the signal at the detector is diminished. Time-domain FT and tunable broadband filter spectrometers concentrate the light on a single or a few detectors, allowing for superior SNR. This SNR enhancement holds when comparing the same measurement bandwidth or, in other words, the same integration time. The enhancement factor depends on the spectrometer configuration, and the specific formalisms can be found elsewhere.[180] It is important to note that this SNR advantage is generally nonexistent when working with a sparse spectrum that only offers a few discrete spectral lines. In the spatially dispersed wavelength multiplexing designs, however, due to the use of broadband filters, the diminished SNR persists even in the case of sparse spectra.

When optical noise spillover becomes significant, time-domain modulated FT and tunable or spatially dispersed multiplexing spectrometers suffer from "Fellgett's disadvantage". When the matrix $G$ is non-diagonal, optical noise from all wavelength channels can impact the measurement. In this case, low-intensity signals can be overshadowed by large photon shot noise from another wavelength with high light intensity, for example, in the case of laser spectroscopy.

## 9 Future Directions

Finally, we discuss the direction in which the field of integrated spectrometry is headed. We first discuss expected developments in terms of spectrometer design, before discussing expected innovation in terms of signal analysis.

Integrated spectrometer designs have moved from classical dispersive and resonator-based designs with a one-to-one correspondence between detector $i$ and spectral channel $j$, towards underdetermined $A$ matrices and computational reconstruction (Sec. 3). Recently, we have seen the emergence of spectrometer designs whose number of optical states $M$ and thus performance metrics scale exponentially. This exponential scaling promises integrated spectrometers with both ultrahigh resolution and ultrabroad bandwidth. Early demonstrations of such architectures, such as the dFT spectrometer,[52] employ optical switches to achieve this exponential scaling ($2^k$ for $k$ switches). More recent work has demonstrated the potential for further enhanced scaling by cascading tunable elements, such as MZIs[124] or MRRs.[118] With $n$ states per tunable element, the scaling factor is increased to $n^k$. We expect this trend to continue, with future breakthroughs in spectrometer designs that allow for exceptional performance improvements with the number of integrated elements.

These types of exponentially scaling spectrometers generally suffer from Fellgett's disadvantage. Co-integration of these spectrometers with additional filters or careful design of the spectrometer's spectral filters can overcome this disadvantage. In the case of laser spectroscopy, for example, the SNR can be significantly improved with a notch filter, filtering out the undesired laser line.

Furthermore, we note that current on-chip spectrometer demonstrations rely heavily on off-chip functionalities. A large portion of the research discussed in this review employs off-chip photodetectors or cameras for data collection. Moreover, the discussed spectrometers generally only collect the data, while post-processing and spectral reconstruction are then performed on a computer. As integrated photonics technology matures, we anticipate that more and more components of the spectrometer will be integrated on-chip.

On-chip/waveguide-integrated photodetectors are an ongoing topic of research.[244,245] Currently, integrated photonic foundries offer Ge photodetectors[246] directly integrated on Si waveguides. Unsurprisingly, a large portion of the spectrometers covered in this review that use on-chip photodetectors employ such Ge-on-Si diodes.[52,139,160,179] Other implementations are based on metal-semiconductor-metal photodetectors,[82] two photon absorption,[156] and single-photon detectors.[87,88] Out of these, on-chip single-photon detectors offer an obvious advantage in terms of SNR. However, the demonstrated spectrometers with single-photon detectors require cryogenic temperatures for operation, limiting the spectrometer's application and increasing

the costs. Integrated avalanche photodetectors offer a promising alternative. These avalanche photodetectors offer sensitivity up to the single-photon level at or near room temperature[247–249] and have been shown for ultraviolet,[250] visible,[249,251] near-IR,[248,252] and mid-IR wavelengths.[253,254]

The next step towards full on-chip integration is the integration of the electronic control and read-out circuit with the photonic circuit. There are two approaches towards this co-integration. In the first approach, for example, proposed by TSMC,[255] an electronic die is directly bonded onto the PIC. The second approach, as, for example, offered at GlobalFoundries,[256] consists of monolithic integration of electronic and photonic circuits onto a single die. As these platforms mature, they will enable true "end-to-end" spectrometer design, where the optical circuit, signal read-out, and signal processing are co-designed and integrated onto a single chip.

Finally, we note that spectrometers have so far mainly focused on direct reconstruction of a discretized equally spaced input spectrum $s$,[51,52] while some works employ radial basis functions[23] (such as Gaussians[116,155]), separation of sparse narrowband and smooth broadband spectral components,[124,166] and neural networks.[117,144] Reconstruction can potentially be improved by exploring other, carefully chosen basis functions for unknown spectra. Additionally, sampling of the input spectrum at unequally spaced wavelength points[35] and various regularization techniques can be explored. Such choices in basis and discretization require prior knowledge of the input spectrum and are likely to be application specific. For applications that rely on spectral information but do not require explicit knowledge of the spectrum itself, one could opt to train a model or neural network to directly perform the task at hand.[107,257]

## Appendix A: Performance Metrics

In this appendix, we provide an overview of the experimentally demonstrated performance metrics for the various categories of integrated photonic spectrometers. Some of the data listed here is plotted in Fig. 9. For each category of integrated photonic spectrometer, a separate table is compiled.

### *A.1 Classical Dispersive Spectrometers*

**Table 2** Overview of Performance Metrics for On-Chip Classical Dispersive Spectrometers[a]

| Ref. | Year | Method | $\lambda_c$ (nm) | $\delta\lambda$ (nm) | $\Delta\lambda$ (nm) | $M$ | $F$ (mm$^2$) | $D$ |
|---|---|---|---|---|---|---|---|---|
| [89] | 2007 | AWG | 1545 | 0.2 | 20 | 50 | 64 | 50 |
| [79] | 2010 | Echelle grating | 1550 | 0.8 | 2.4 | 3 | 24 | 3 |
| [94] | 2010 | PhC grating | 1560 | 2.5 | 55 | 22 | 0.384 | 22 |
| [80] | 2013 | AWG | 3800 | 9.6 | 77 | 6 | 0.75 | 6 |
| [80] | 2013 | Echelle grating | 3800 | 10 | 105 | 8 | 3.06 | 8 |
| [81] | 2013 | Echelle grating | 1550 | 3.2 | 115 | 8 | 0.56 | 8 |
| [81] | 2013 | Echelle grating | 1650 | 7 | 121 | 14 | 0.24 | 14 |
| [81] | 2013 | Echelle grating | 2125 | 6 | 150 | 16 | 0.54 | 16 |
| [81] | 2013 | Echelle grating | 2320 | 5 | 60 | 8 | 1.04 | 8 |
| [81] | 2013 | AWG | 2200 | 1.6 | 13 | 6 | 1 | 6 |
| [81] | 2013 | AWG | 2200 | 4.8 | 38 | 6 | 0.48 | 6 |
| [82] | 2013 | Echelle grating | 850 | 0.5 | 30 | 60 | 54 | 60 |
| [83] | 2014 | Echelle grating | 1550 | 12.7 | 125 | 15 | 4 | 15 |
| [95] | 2014 | Planar holograms | 740 | 0.15 | 148 | 926 | 200 | 926 |
| [96] | 2014 | Hologram + interferometers | 790 | 0.145 | 142 |  | 20 |  |
| [90] | 2016 | AWG | 760 | 0.5 | 4 | 8 | 2.8 | 8 |
| [91] | 2017 | AWG | 1550 | 1.6 | 9 | 5 | 112 | 5 |
| [84] | 2018 | Echelle grating | 1550 | 0.5 | 60 | 121 | 9 | 121 |
| [85] | 2018 | Echelle grating | 1545 | 4.9 | 25 | 5 | 2.25 | 5 |
| [86] | 2019 | Echelle grating | 1300 | 4.5 | 18 | 4 | 0.02 | 4 |
| [87] | 2019 | Echelle grating | 1300 | 7 | 1400 |  | 4 |  |
| [87] | 2019 | Echelle grating | 1550 | 2.5 | 160 |  |  |  |
| [92] | 2019 | AWG | 860 | 1.5 | 60 | 40 | 0.62 | 40 |
| [93] | 2020 | Cascaded AWGs | 1550 | 1 | 195 | 195 | 110 | 195 |
| [88] | 2023 | Echelle grating | 1505 | 0.4 | 20 | 16 | 0.2 | 16 |
| [98] | 2023 | Metalenses | 1550 | 0.14 | 50 | 32 | 0.01 | 32 |

[a]For each example, the year of publication of the referenced paper, implementation method, center wavelength $\lambda_c$, spectral resolution $\delta\lambda$, bandwidth $\Delta\lambda$, number of measurements $M$, footprint $F$, and number of detectors $D$ are listed.

### *A.2 Resonator Array Spectrometers*

**Table 3** Overview of Performance Metrics for On-Chip Resonator Array Spectrometers[a]

| Ref. | Year | Method | $\lambda_c$ (nm) | $\delta\lambda$ (nm) | $\Delta\lambda$ (nm) | $M$ | $F$ (mm$^2$) | $D$ |
|---|---|---|---|---|---|---|---|---|
| [99] | 2011 | MRR | 1580 | 0.6 | 50 | 84 | 1 | 84 |
| [100] | 2012 | PhC cavity | 840 | 0.3 | 35 | 100 | 0.004 | 100 |
| [126] | 2021 | MRR + AWG | 860 | 0.75 | 57.5 | 70 | 1.4 | 70 |
| [129] | 2021 | PhC cavity | 1580 | 5 | 70 | 38 | 0.0007 | 38 |
| [128] | 2022 | MRR | 3410 | 23 | 90 | 4 | 0.01 | 4 |
| [101] | 2023 | MRR | 809 | 0.17 | 12 | 3 | 0.15 | 3 |

[a]For each example, the year of publication of the referenced paper, implementation method, center wavelength $\lambda_c$, spectral resolution $\delta\lambda$, bandwidth $\Delta\lambda$, number of measurements $M$, footprint $F$, and number of detectors $D$ are listed.

### *A.3 Wavelength Multiplexing Spectrometers*

**Table 4** Overview of Performance Metrics for Spatially Dispersed Wavelength Multiplexing Spectrometers[a]

| Ref. | Year | Method | $\lambda_c$ (nm) | $\delta\lambda$ (nm) | $\Delta\lambda$ (nm) | $M$ | $F$ (mm$^2$) | $D$ |
|---|---|---|---|---|---|---|---|---|
| [57] | 2013 | Scattering | 1512 | 0.75 | 25 | 33 | 0.005 | 33 |
| [133] | 2013 | FT | 1550 | 0.04 | 0.75 | 32 | 12 | 18 |
| [134] | 2013 | FT | 1550 | 0.05 | 2 | 32 | 24 | 32 |
| [135] | 2015 | FT | 3750 | 2.7 | 54 | 42 | 95 | 42 |
| [102] | 2016 | Multimode spiral | 1520 | 0.01 | 2 | 40 | 0.25 | 40 |
| [51] | 2017 | FT | 1550 | 0.03 | 0.78 | 14 |  | 14 |
| [136] | 2017 | FT | 1400 | 4.8 | 600 | 201 | 165 | 201 |
| [137] | 2019 | FT | 1550 | 0.038 | 0.5 | 34 | 4.75 | 34 |
| [103] | 2020 | Speckle-enhanced FT | 1556 | 0.003 | 12 | 640 | 100 | 640 |
| [132] | 2020 | Scattering | 755 | 0.3 | 15 | 13 | 0.02 | 13 |
| [132] | 2020 | Scattering | 955 | 1 | 15 | 13 | 0.02 | 13 |
| [132] | 2020 | Scattering | 1550 | 3 | 40 | 13 | 0.02 | 13 |
| [104] | 2021 | Scattering | 1556 | 0.25 | 30 | 8 | 0.0004 | 8 |
| [105] | 2021 | Stratified waveguides | 1560 | 0.45 | 180 | 32 | 0.009 | 32 |
| [106] | 2021 | Coherent network | 776 | 0.02 | 12 | 8 | 0.11 | 8 |
| [139] | 2021 | FT | 1568 | 0.09 | 0.6 | 16 | 4.5 | 16 |
| [140] | 2021 | FT | 1460 | 0.05 | 340 | 16 | 10 | 16 |
| [141] | 2022 | FT | 850 | 3.4 | 400 | 32 | 3.06 | 32 |
| [107] | 2023 | Disordered lattice | 1545 | 0.015 | 40 | 4096 | 1 | 4096 |
| [142] | 2023 | FT | 1560 | 0.4 | 7 | 32 | 27 | 32 |
| [143] | 2023 | FT | 1550 | 3 | 35 | 16 | 1.64 | 16 |
| [146] | 2023 | Coherent network | 1520 | 0.1 | 10 | 25 | 0.026 | 5 |
| [147] | 2023 | Self-coupled waveguides | 1550 | 0.1 | 100 | 64 | 3 | 64 |
| [144] | 2024 | Multimode interference | 795 | 1 | 40 |  | 0.625 |  |
| [144] | 2024 | Multimode interference | 795 | 0.05 | 2 | 144000 |  | 144000 |
| [145] | 2025 | Multimode interference | 1570 | 0.1 | 30 | 12 | 0.0003 | 12 |
| [148] | 2025 | Metasurfaces | 1550 | 0.047 | 40 | 1200 | 0.045 | 1200 |

[a]For each example, the year of publication of the referenced paper, implementation method, center wavelength $\lambda_c$, spectral resolution $\delta\lambda$, bandwidth $\Delta\lambda$, number of measurements $M$, footprint $F$, and number of detectors $D$ are listed.

### *A.4 Stationary-Wave Integrated Fourier-Transform Spectrometers*

**Table 5** Overview of Performance Metrics for Stationary-Wave Integrated Fourier-Transform Spectrometers[a]

| Ref. | Year | Method | $\lambda_c$ (nm) | $\delta\lambda$ (nm) | $\Delta\lambda$ (nm) | $M$ | $F$ (mm$^2$) | $D$ |
|---|---|---|---|---|---|---|---|---|
| [150] | 2017 | Copropagative | 900 | 6 | 100 | | 0.1 | |
| [108] | 2018 | Lippmann | 633 | 0.16 | 256 | 2000 | 0.032 | 2000 |
| [109] | 2018 | Tunable SWIFTS | 1500 | 40 | 1000 | 347 | 0.001 | 5 |
| [153] | 2020 | Tunable SWIFTS | 1550 | 5.5 | 500 | | 10 | 87 |
| [110] | 2024 | Lippmann | 842.5 | 0.2 | 75 | 160 | 5.12 | 160 |

[a]For each example, the year of publication of the referenced paper, implementation method, center wavelength $\lambda_c$, spectral resolution $\delta\lambda$, bandwidth $\Delta\lambda$, number of measurements $M$, footprint $F$, and number of detectors $D$ are listed.

### *A.5 Tunable Narrowband Filter Spectrometers*

**Table 6** Overview of Performance Metrics for On-Chip Tunable Narrowband Filter Spectrometers[a]

| Ref. | Year | Method | $\lambda_c$ (nm) | $\delta\lambda$ (nm) | $\Delta\lambda$ (nm) | $M$ | $F$ (mm$^2$) | $D$ |
|---|---|---|---|---|---|---|---|---|
| [159] | 2010 | MRR + AWG | 1488 | 0.1 | 10 | 100 | 2 | 25 |
| [111] | 2016 | MRR | 1580 | 0.15 | 19 | 126 | 0.6 | 1 |
| [160] | 2019 | MRR + AWG | 1555 | 0.1 | 25.4 | 254 | 9 | 9 |
| [112] | 2022 | PhC cavity | 1455 | 0.5 | 12.3 | 25 | | 1 |
| [113] | 2022 | FP cavity array | 1472 | 0.43 | 73.2 | 170 | 0.026 | 5 |
| [113] | 2022 | FP cavity array | 1472 | 0.51 | 102.7 | 201 | 0.036 | 7 |
| [114] | 2022 | MRR + MRR array | 1550 | 0.005 | 9.7 | 17389 | 0.35 | 11 |
| [155] | 2022 | PhC cavity | 1556 | 0.32 | 16 | 100 | 0.0045 | 3 |
| [161] | 2022 | MRR + AWG | 1300 | 0.2 | 70 | 350 | 0.12 | 10 |
| [115] | 2023 | Photonic molecule | 1550 | 0.04 | 100 | 2501 | 0.004 | 1 |
| [116] | 2023 | Microdisk | 1505 | 0.01 | 0.3 | 65 | 0.24 | 1 |
| [116] | 2023 | Microdisk | 1510 | 0.2 | 20 | 321 | 0.24 | 1 |
| [166] | 2023 | Multimode MRR | 1550 | 0.08 | 100 | 1250 | 0.0007 | 2 |
| [117] | 2024 | Cascaded MRRs | 1550 | 0.1 | 200 | 2187 | 0.004 | 3 |
| [117] | 2024 | Cascaded MRRs | 1550 | 2 | 200 | 192 | 0.004 | 3 |
| [118] | 2024 | Cascaded MRRs | 1440 | 0.008 | 520 | 4096 | 0.6 | 1 |
| [156] | 2024 | MRR | 1550 | 0.4 | 10 | | 0.0003 | 1 |
| [157] | 2024 | MRR + lattice filter | 1550 | 0.2 | 35 | | 1.9 | 8 |
| [158] | 2025 | MRR + lattice filter | 1550 | 0.2 | 40 | | 0.21 | 4 |

[a]For each example, the year of publication of the referenced paper, implementation method, center wavelength $\lambda_c$, spectral resolution $\delta\lambda$, bandwidth $\Delta\lambda$, number of measurements $M$, footprint $F$, and number of detectors $D$ are listed.

### *A.6 Fourier-Transform Spectrometers*

**Table 7** Overview of Performance Metrics for On-Chip Fourier-Transform Spectrometers[a]

| Ref. | Year | Method | $\lambda_c$ (nm) | $\delta\lambda$ (nm) | $\Delta\lambda$ (nm) | $M$ | $F$ (mm$^2$) | $D$ |
|---|---|---|---|---|---|---|---|---|
| [167] | 2014 | Lithium niobate | 1550 | 68 | 450 | | | 1 |
| [52] | 2018 | dFT | 1560 | 0.2 | 20 | 64 | 1.9 | 1 |
| [169] | 2018 | Thermo-optic | 1550 | 3.0 | 56 | 18 | 1 | 1 |
| [120] | 2019 | MRR assisted TO | 1571 | 0.47 | 90 | | | 1 |
| [170] | 2019 | Thermo-optic | 7700 | 79 | 2900 | | | |
| [175] | 2019 | dFT | 2300 | 0.1 | 130 | 64 | 5.3 | |
| [119] | 2020 | Thermo-optic | 1550 | 0.9 | 56 | 63 | 0.9 | 1 |
| [172] | 2020 | MEMS | 1550 | 2.7 | 20 | | 108 | 4 |
| [173] | 2021 | Spatial heterodyne TO | 1560 | 0.16 | 130 | | | 3 |
| [177] | 2022 | dFT | 1552 | 0.02 | 3 | 127 | | |
| [121] | 2024 | MEMS | 1550 | 0.2 | 100 | 53 | 0.075 | 1 |
| [121] | 2024 | MEMS | 4150 | 1.5 | 300 | 53 | | 1 |
| [122] | 2024 | 2D FT | 1550 | 0.13 | 200 | | | 128 |
| [168] | 2024 | Lithium niobate | 1550 | 5.3 | 100 | | | 1 |
| [178] | 2024 | dFT | 3875 | 8 | 450 | 128 | | 1 |

[a]For each example, the year of publication of the referenced paper, implementation method, center wavelength $\lambda_c$, spectral resolution $\delta\lambda$, bandwidth $\Delta\lambda$, number of measurements $M$, footprint $F$, and number of detectors $D$ are listed.

### *A.7 Tunable Broadband Filter Spectrometers*

**Table 8** Overview of Performance Metrics for On-Chip Tunable Broadband Filter Spectrometers[a]

| Ref. | Year | Method | $\lambda_c$ (nm) | $\delta\lambda$ (nm) | $\Delta\lambda$ (nm) | $M$ | $F$ (mm$^2$) | $D$ |
|---|---|---|---|---|---|---|---|---|
| [123] | 2017 | Multimode spiral | 1554 | 0.015 | 2 | 144 | 3.36 | 12 |
| [179] | 2021 | Multimode interference | 1565 | 0.3 | 6.4 | 64 | | 4 |
| [182] | 2022 | Multimode interference | 1590 | 0.02 | 100 | 384 | 1.5 | 6 |
| [124] | 2023 | MZIs | 1510 | 0.01 | 200 | 729 | 8 | 1 |
| [125] | 2023 | Cavity-enhanced mode mixing | 1550 | 0.005 | 100 | 2001 | 1.5 | 1 |
| [183] | 2023 | Coherent network | 1559 | 0.03 | 115 | 256 | 16.65 | 4 |
| [181] | 2024 | Coherent network | 1520 | 0.01 | 120 | 400 | 0.5 | 1 |
| [181] | 2024 | Coherent network | 1520 | 0.3 | 120 | 132 | 0.5 | 1 |
| [184] | 2025 | Beam-steered metasurfaces | 1560 | 0.07 | 100 | 1200 | 0.1425 | |

[a]For each example, the year of publication of the referenced paper, implementation method, center wavelength $\lambda_c$, spectral resolution $\delta\lambda$, bandwidth $\Delta\lambda$, number of measurements $M$, footprint $F$, and number of detectors $D$ are listed.

## *Acknowledgments*

We acknowledge funding support provided by the NASA STTR contract 80NSSC23CA018, the NSF Award 2122581, the US Army Research Office through the Institute for Soldier Nanotechnologies Award W911NF-23-2-0121, and the Simons Foundation through the Simons Collaboration on Extreme Wave Phenomena Based on Symmetries.

## *References*

1. C. P. Bacon, Y. Mattley, and R. DeFrece, "Miniature spectroscopic instrumentation: applications to biology and chemistry," *Rev. Sci. Instrum.* **75**, 1 (2004).
2. R. A. Crocombe, Handheld spectrometers: the state of the art, in *Next-Generation Spectroscopic Technologies VI*, Vol. **8726** (2013), p. 174.

3. S. Di Nonno and R. Ulber, "Smartphone-based optical analysis systems," *Analyst* **146**, 2749 (2021).
4. R. A. Crocombe, Miniature and multi-spectral spectrometers in consumer goods and wearables, in *MOEMS and Miniaturized Systems XXII*, Vol. **12434** (2023), p. 50.
5. M. J. Heck *et al.*, "Hybrid silicon photonic integrated circuit technology," *IEEE J. Sel. Top. Quantum Electron.* **19**, 6100117 (2012).
6. R. Wang *et al.*, "III–V-on-silicon photonic integrated circuits for spectroscopic sensing in the 2–4 μm wavelength range," *Sensors* **17**, 1788 (2017).
7. H. Lin *et al.*, "Mid-infrared integrated photonics on silicon: a perspective," *Nanophotonics* **7**, 393 (2017).
8. T. Sharma *et al.*, "Review of recent progress on silicon nitride-based photonic integrated circuits," *IEEE Access* **8**, 195436 (2020).
9. F. Gardes *et al.*, "A review of capabilities and scope for hybrid integration offered by silicon-nitride-based photonic integrated circuits," *Sensors* **22**, 4227 (2022).
10. M. J. Heck *et al.*, "Ultra-low loss waveguide platform and its integration with silicon photonics," *Laser Photonics Rev.* **8**, 667 (2014).
11. D. M. Kita *et al.*, "On-chip infrared spectroscopic sensing: redefining the benefits of scaling," *IEEE J. Sel. Top. Quantum Electron.* **23**, 340 (2017).
12. Z. Yang *et al.*, "Miniaturization of optical spectrometers," *Science* **371**, eabe0722 (2021).
13. A. Li *et al.*, "Advances in cost-effective integrated spectrometers," *Light Sci. Appl.* **11**, 174 (2022).
14. K. B. Beć, J. Grabska, and C. W. Huck, "Principles and applications of miniaturized near-infrared (NIR) spectrometers," *Chem.–A Eur. J.* **27**, 1514 (2021).
15. W. Wei-ping and J. Li, "Research progress of on-chip spectrometer based on the silicon photonics platform," *Spectros. Spectral Anal.* **40**, 333 (2020).
16. A. Ravindran *et al.*, "Optical grating techniques for MEMS-based spectrometer—a review," *IEEE Sens. J.* **21**, 5645 (2020).
17. L. Gao *et al.*, "Computational spectrometers enabled by nanophotonics and deep learning," *Nanophotonics* **11**, 2507 (2022).
18. K. Atkinson, *An Introduction to Numerical Analysis* (John Wiley & Sons, 1991).
19. P. J. Davis and P. Rabinowitz, *Methods of Numerical Integration* (Dover Publications, 2007).
20. L. N. Trefethen, *Approximation Theory and Approximation Practice* (SIAM, 2019).
21. R. G. Bartle and D. R. Sherbert, *Introduction to Real Analysis* (John Wiley & Sons, 2011).
22. S. Abbott, *Understanding Analysis* (Springer, 2015).
23. M. D. Buhmann, *Radial Basis Functions: Theory and Implementations* (Cambridge University Press, 2003).
24. C.-C. Chang *et al.*, "Spectrum reconstruction for filter-array spectrum sensor from sparse template selection," *Opt. Eng.* **50**, 114402 (2011).
25. C.-C. Chang *et al.*, "A sparse template selection algorithm for spectrum measurement using miniature filter array spectrum sensors," in *2012 7th IEEE Conference on Industrial Electronics and Applications (ICIEA)*, Vol. **17** (IEEE, 2012), p. 437.
26. Z. Yang *et al.*, "Single-nanowire spectrometers," *Science* **365**, 1017 (2019).
27. C. C. Aggarwal, *Neural Networks and Deep Learning* (Springer, 2018).
28. C. Brown *et al.*, "Neural network-based on-chip spectroscopy using a scalable plasmonic encoder," *ACS Nano* **15**, 6305 (2021).
29. L. Yang *et al.*, "A lightweight neural network compatible with high-correlation broadband optical filters in computational spectroscopy," *Opt. Lasers Eng.* **167**, 107630 (2023).
30. H. Liao *et al.*, "A neural network computational spectrometer trained by a small dataset with high-correlation optical filters," *Sensors* **24**, 1553 (2024).
31. Z. Wang *et al.*, "Opto-intelligence spectrometer using diffractive neural networks," *Nanophotonics* **13**, 3883 (2024).
32. J. Wang *et al.*, "Miniaturized spectrometer based on MLP neural networks and a frosted glass encoder," *Opt. Express* **32**, 30632 (2024).
33. J. Liang *et al.*, "Lensless speckle reconstructive spectrometer via physics-aware neural network," arXiv:2412.18238 (2024).
34. L. N. Trefethen and D. Bau, *Numerical Linear Algebra* (SIAM, 2022).
35. W. Ma *et al.*, "Inverse design for robust inference in integrated computational spectrometry," arXiv:2506.02194 (2025).
36. G. Wetzstein *et al.*, "Inference in artificial intelligence with deep optics and photonics," *Nature* **588**, 39 (2020).
37. V. Sitzmann *et al.*, "End-to-end optimization of optics and image processing for achromatic extended depth of field and super-resolution imaging," *ACM Trans. Graph.* **37**, 1 (2018).
38. Q. Sun *et al.*, "End-to-end learned, optically coded super-resolution SPAD camera," *ACM Trans. Graph.* **39**, 1 (2020).
39. E. Tseng *et al.*, "Differentiable compound optics and processing pipeline optimization for end-to-end camera design," *ACM Trans. Graph.* **40**, 1 (2021).
40. Z. Lin *et al.*, "End-to-end nanophotonic inverse design for imaging and polarimetry," *Nanophotonics* **10**, 1177 (2021).
41. Z. Lin *et al.*, "End-to-end metasurface inverse design for single-shot multi-channel imaging," *Opt. Express* **30**, 28358 (2022).
42. W. F. Li *et al.*, "Transcending shift-invariance in the paraxial regime via end-to-end inverse design of freeform nanophotonics," *Opt. Express* **31**, 24260 (2023).
43. G. Arya *et al.*, "End-to-end optimization of metasurfaces for imaging with compressed sensing," *ACS Photonics* **11**, 2077 (2024).
44. U. Kurokawa, B. I. Choi, and C.-C. Chang, "Filter-based miniature spectrometers: Spectrum reconstruction using adaptive regularization," *IEEE Sens. J.* **11**, 1556 (2011).
45. T. Yang *et al.*, "Novel high resolution miniature spectrometer using an integrated diffraction hole array," in *2012 17th Opto-Electronics and Communications Conference* (IEEE, 2012), p. 865.
46. T. Yang *et al.*, "An ultra compact spectrometer based on the optical transmission through a micro interferometer array," *Optik* **124**, 1377 (2013).
47. J. Oliver *et al.*, "Improving resolution of miniature spectrometers by exploiting sparse nature of signals," *Opt. Express* **20**, 2613 (2012).
48. Y. August and A. Stern, "Compressive sensing spectrometry based on liquid crystal devices," *Opt. Lett.* **38**, 4996 (2013).
49. Z. Wang and Z. Yu, "Spectral analysis based on compressive sensing in nanophotonic structures," *Opt. Express* **22**, 25608 (2014).
50. S. F. Liew *et al.*, "Broadband multimode fiber spectrometer," *Opt. Lett.* **41**, 2029 (2016).
51. H. Podmore *et al.*, "Demonstration of a compressive-sensing Fourier-transform on-chip spectrometer," *Opt. Lett.* **42**, 1440 (2017).
52. D. M. Kita *et al.*, "High-performance and scalable on-chip digital Fourier transform spectroscopy," *Nat. Commun.* **9**, 4405 (2018).
53. P. C. Hansen, V. Pereyra, and G. Scherer, *Least Squares Data Fitting with Applications* (JHU Press, 2013).
54. G. Strang, *Linear Algebra and Learning from Data* (SIAM, 2019).
55. Z. Xu *et al.*, "Multimodal multiplex spectroscopy using photonic crystals," *Opt. Express* **11**, 2126 (2003).

56. C.-C. Chang and H.-N. Lee, "On the estimation of target spectrum for filter-array based spectrometers," *Opt. Express* **16**, 1056 (2008).
57. B. Redding *et al.*, "Compact spectrometer based on a disordered photonic chip," *Nat. Photonics* **7**, 746 (2013).
58. B. Redding, S. M. Popoff, and H. Cao, "All-fiber spectrometer based on speckle pattern reconstruction," *Opt. Express* **21**, 6584 (2013).
59. P. Wang and R. Menon, "Computational spectrometer based on a broadband diffractive optic," *Opt. Express* **22**, 14575 (2014).
60. S. Boyd and L. Vandenberghe, *Convex Optimization*, Cambridge University Press (2004).
61. D. Chen and R. J. Plemmons, "Nonnegativity constraints in numerical analysis," in *The Birth of Numerical Analysis*, (World Scientific, 2010), p. 109.
62. A. Ben-Tal and A. Nemirovski, *Lectures on Modern Convex Optimization: Analysis, Algorithms, and Engineering Applications* (SIAM, 2001).
63. D. Brooks *et al.*, "Inverse electrocardiography by simultaneous imposition of multiple constraints," *IEEE Trans. Biomed. Eng.* **46**, 3 (1999).
64. P. C. Hansen, *Rank-Deficient and Discrete Ill-Posed Problems: Numerical Aspects of Linear Inversion* (Society for Industrial and Applied Mathematics, 1998).
65. Q. Hang *et al.*, "Photonic bandgap fiber bundle spectrometer," *Appl. Opt.* **49**, 4791 (2010).
66. J. E. Jackson, *A User's Guide to Principal Components* (John Wiley & Sons, 2005).
67. S. Foucart and H. Rauhut, *A Mathematical Introduction to Compressive Sensing* (Springer, 2013).
68. T. J. Hastie, R. J. Tibshirani, and M. J. Wainwright, *Statistical Learning with Sparsity: The Lasso and Generalizations* (CRC Press, 2015).
69. S. Shalev-Shwartz and S. Ben-David, *Understanding Machine Learning: From Theory to Algorithms* (Cambridge University Press, 2014).
70. M. Mohri, *Foundations of Machine Learning* (MIT Press, 2018).
71. G. James *et al.*, *An Introduction to Statistical Learning: with Applications in R* (Springer US, 2021).
72. I. Tošić and P. Frossard, "Dictionary learning," *IEEE Signal Process Mag.* **28**, 27 (2011).
73. S. Zhang *et al.*, "A spectral reconstruction algorithm of miniature spectrometer based on sparse optimization and dictionary learning," *Sensors* **18**, 644 (2018).
74. J. Zhang *et al.*, "A survey on computational spectral reconstruction methods from RGB to hyperspectral imaging," *Sci. Rep.* **12**, 11905 (2022).
75. A. Kazerouni *et al.*, "Diffusion models in medical imaging: a comprehensive survey," *Med. Image Anal.* **88**, 102846 (2023).
76. G. Webber and A. J. Reader, "Diffusion models for medical image reconstruction," *BJR\Artificial Intelligence* **1**, ubae013 (2024).
77. D. Jakubovitz, R. Giryes, and M. R. D. Rodrigues, *Generalization Error in Deep Learning*, (Springer International Publishing, 2019), p. 153.
78. Y. Wang *et al.*, "Generalizing from a few examples: a survey on few-shot learning," *ACM Comput. Surv.* **53**, 1 (2020).
79. J. Song and J. F. Ding, "Echelle diffraction grating demultiplexers with a single diffraction passband," *Opt. Commun.* **283**, 537 (2010).
80. M. Muneeb *et al.*, "Demonstration of silicon-on-insulator mid-infrared spectrometers operating at 3.8 μm," *Opt. Express* **21**, 11659 (2013).
81. E. Ryckeboer *et al.*, "Silicon-on-insulator spectrometers with integrated GaInAsSb photodiodes for wide-band spectroscopy from 1510 to 2300 nm," *Opt. Express* **21**, 6101 (2013).
82. X. Ma, M. Li, and J.-J. He, "CMOS-compatible integrated spectrometer based on echelle diffraction grating and MSM photodetector array," *IEEE Photonics J.* **5**, 6600807 (2013).
83. P. Pottier, M. J. Strain, and M. Packirisamy, "Integrated microspectrometer with elliptical Bragg mirror enhanced diffraction grating on silicon on insulator," *ACS Photonics* **1**, 430 (2014).
84. K. Ma *et al.*, "High-resolution compact on-chip spectrometer based on an echelle grating with densely packed waveguide array," *IEEE Photonics J.* **11**, 1 (2018).
85. S. Xie, Y. Meng, J. Bland-Hawthorn *et al.*, "Silicon nitride/silicon dioxide echelle grating spectrometer for operation near 1.55 μm," *IEEE Photonics J.* **10**, 1 (2018).
86. D. Melati *et al.*, "Compact and low crosstalk echelle grating demultiplexer on silicon-on-insulator technology," *Electronics* **8**, 687 (2019).
87. R. Cheng *et al.*, "Broadband on-chip single-photon spectrometer," *Nat. Commun.* **10**, 4104 (2019).
88. J. Zheng *et al.*, "An on-chip photon-counting reconstructive spectrometer with tailored cascaded detector array," *Adv. Dev. Instrum.* **4**, 0021 (2023).
89. P. Cheben *et al.*, "A high-resolution silicon-on-insulator arrayed waveguide grating microspectrometer with sub-micrometer aperture waveguides," *Opt. Express* **15**, 2299 (2007).
90. E. Stanton *et al.*, "Low-loss arrayed waveguide grating at 760 nm," *Opt. Lett.* **41**, 1785 (2016).
91. P. Gatkine *et al.*, "Arrayed waveguide grating spectrometers for astronomical applications: new results," *Opt. Express* **25**, 17918 (2017).
92. Z. Zhang, Y. Wang, and H. K. Tsang, "Ultracompact 40-channel arrayed waveguide grating on silicon nitride platform at 860 nm," *IEEE J. Quantum Electron.* **56**, 1 (2019).
93. A. van Wijk *et al.*, "Compact ultrabroad-bandwidth cascaded arrayed waveguide gratings," *Opt. Express* **28**, 14618 (2020).
94. B. Momeni *et al.*, "An on-chip silicon grating spectrometer using a photonic crystal reflector," *J. Opt.* **12**, 035501 (2010).
95. G. Calafiore *et al.*, "Holographic planar lightwave circuit for on-chip spectroscopy," *Light Sci. Appl.* **3**, e203 (2014).
96. A. Koshelev *et al.*, "Combination of a spectrometer-on-chip and an array of Young's interferometers for laser spectrum monitoring," *Opt. Lett.* **39**, 5645 (2014).
97. J. Upham *et al.*, "Realization of a flat-band superprism on-chip from parallelogram lattice photonic crystals," *Opt. Lett.* **43**, 4981 (2018).
98. Z. Zhang *et al.*, "Folded digital meta-lenses for on-chip spectrometer," *Nano Lett.* **23**, 3459 (2023).
99. Z. Xia *et al.*, "High resolution on-chip spectroscopy based on miniaturized microdonut resonators," *Opt. Express* **19**, 12356 (2011).
100. X. Gan *et al.*, "A high-resolution spectrometer based on a compact planar two dimensional photonic crystal cavity array," *Appl. Phys. Lett.* **100**, 231104 (2012).
101. X. Chen *et al.*, "On-chip micro-ring resonator array spectrum detection system based on convex optimization algorithm," *Nanophotonics* **12**, 715 (2023).
102. B. Redding *et al.*, "Evanescently coupled multimode spiral spectrometer," *Optica* **3**, 956 (2016).
103. U. Paudel and T. Rose, "Ultra-high resolution and broadband chip-scale speckle enhanced Fourier-transform spectrometer," *Opt. Express* **28**, 16469 (2020).
104. W. Hadibrata *et al.*, "Compact, high-resolution inverse-designed on-chip spectrometer based on tailored disorder modes," *Laser Photonics Rev.* **15**, 2000556 (2021).
105. A. Li and Y. Fainman, "On-chip spectrometers using stratified waveguide filters," *Nat. Commun.* **12**, 2704 (2021).
106. Z. Zhang *et al.*, "Compact high resolution speckle spectrometer by using linear coherent integrated network on silicon nitride platform at 776 nm," *Laser Photonics Rev.* **15**, 2100039 (2021).
107. Z. Lin *et al.*, "High-performance, intelligent, on-chip speckle spectrometer using 2D silicon photonic disordered microring lattice," *Optica* **10**, 497 (2023).

108. M. Madi *et al.*, "Lippmann waveguide spectrometer with enhanced throughput and bandwidth for space and commercial applications," *Opt. Express* **26**, 2682 (2018).
109. J. Loridat *et al.*, "All integrated lithium niobate standing wave Fourier transform electro-optic spectrometer," *J. Lightwave Technol.* **36**, 4900 (2018).
110. S. Kerman *et al.*, "Scalable miniature on-chip Fourier transform spectrometer for Raman spectroscopy," *Light Sci. Appl.* **14**, 208 (2025).
111. S. Zheng *et al.*, "High-resolution on-chip spectrometer with a tunable micro-ring resonator filter," in *CLEO: Applications and Technology, AM1J–2* (Optica Publishing Group, 2016).
112. C. Sun *et al.*, "Tunable narrow-band single-channel add-drop integrated optical filter with ultrawide FSR," *PhotoniX* **3**, 12 (2022).
113. C. Sun *et al.*, "Broadband and high-resolution integrated spectrometer based on a tunable FSR-free optical filter array," *ACS Photonics* **9**, 2973 (2022).
114. L. Zhang *et al.*, "Ultrahigh-resolution on-chip spectrometer with silicon photonic resonators," *Opto-Electron. Adv.* **5**, 210100 (2022).
115. H. Xu *et al.*, "Breaking the resolution-bandwidth limit of chip-scale spectrometry by harnessing a dispersion-engineered photonic molecule," *Light Sci. Appl.* **12**, 64 (2023).
116. C. Sun *et al.*, "Scalable on-chip microdisk resonator spectrometer," *Laser Photonics Rev.* **17**, 2200792 (2023).
117. Z. Zhang *et al.*, "On-chip reconstructive spectrometer based on parallel cascaded micro-ring resonators," *Appl. Sci.* **14**, 4886 (2024).
118. C. Yao *et al.*, "Chip-scale sensor for spectroscopic metrology," *Nat. Commun.* **15**, 10305 (2024).
119. A. Li *et al.*, "Fabrication-tolerant Fourier transform spectrometer on silicon with broad bandwidth and high resolution," *Photonics Res.* **8**, 219 (2020).
120. S. N. Zheng *et al.*, "Microring resonator-assisted Fourier transform spectrometer with enhanced resolution and large bandwidth in single chip solution," *Nat. Commun.* **10**, 2349 (2019).
121. H. Chen *et al.*, "High-performance and wavelength-transplantable on-chip Fourier transform spectrometer using MEMS in-plane reconfiguration," *Photonics Res.* **12**, 1730 (2024).
122. H. Xu *et al.*, "Scalable integrated two-dimensional Fourier-transform spectrometry," *Nat. Commun.* **15**, 436 (2024).
123. M. Piels and D. Zibar, "Compact silicon multimode waveguide spectrometer with enhanced bandwidth," *Sci. Rep.* **7**, 43454 (2017).
124. C. Yao *et al.*, "Integrated reconstructive spectrometer with programmable photonic circuits," *Nat. Commun.* **14**, 6376 (2023).
125. H. Xu *et al.*, "Cavity-enhanced scalable integrated temporal random-speckle spectrometry," *Optica* **10**, 1177 (2023).
126. Z. Zhang, Y. Wang, and H. K. Tsang, "Tandem configuration of microrings and arrayed waveguide gratings for a high-resolution and broadband stationary optical spectrometer at 860 nm," *ACS Photonics* **8**, 1251 (2021).
127. T. S. Karnik *et al.*, "High-efficiency mid-infrared InGaAs/InP arrayed waveguide gratings," *Opt. Express* **31**, 5056 (2023).
128. J. Zhou *et al.*, "Mid-infrared serial microring resonator array for real-time detection of vapor-phase volatile organic compounds," *Anal. Chem.* **94**, 11008 (2022).
129. Z. Cheng *et al.*, "Generalized modular spectrometers combining a compact nanobeam microcavity and computational reconstruction," *ACS Photonics* **9**, 74 (2021).
130. D. Liu *et al.*, "Silicon photonic filters," *Microw. Opt. Technol. Lett.* **63**, 2252 (2021).
131. B. Redding and H. Cao, "Using a multimode fiber as a high-resolution, low-loss spectrometer," *Opt. Lett.* **37**, 3384 (2012).
132. W. Hartmann *et al.*, "Waveguide-integrated broadband spectrometer based on tailored disorder," *Adv. Opt. Mater.* **8**, 1901602 (2020).
133. A. V. Velasco *et al.*, "High-resolution Fourier-transform spectrometer chip with microphotonic silicon spiral waveguides," *Opt. Lett.* **38**, 706 (2013).
134. P. J. Bock *et al.*, "Subwavelength grating Fourier-transform interferometer array in silicon-on-insulator," *Laser Photonics Rev.* **7**, L67 (2013).
135. M. Nedeljkovic *et al.*, "Mid-infrared silicon-on-insulator Fourier-transform spectrometer chip," *IEEE Photonics Technol. Lett.* **28**, 528 (2015).
136. M. Yang, M. Li, and J.-J. He, "Static FT imaging spectrometer based on a modified waveguide MZI array," *Opt. Lett.* **42**, 2675 (2017).
137. H. Wang *et al.*, "On-chip Fourier transform spectrometers by dual-polarized detection," *Opt. Lett.* **44**, 2923 (2019).
138. A. Herrero-Bermello *et al.*, "On-chip Fourier-transform spectrometers and machine learning: a new route to smart photonic sensors," *Opt. Lett.* **44**, 5840 (2019).
139. T. T. D. Dinh *et al.*, "Silicon photonic on-chip spatial heterodyne Fourier transform spectrometer exploiting the Jacquinot's advantage," *Opt. Lett.* **46**, 1341 (2021).
140. D. González-Andrade *et al.*, "Broadband Fourier-transform silicon nitride spectrometer with wide-area multiaperture input," *Opt. Lett.* **46**, 4021 (2021).
141. K. M. Yoo and R. T. Chen, "Dual-polarization bandwidth-bridged bandpass sampling Fourier transform spectrometer from visible to near-infrared on a silicon nitride platform," *ACS Photonics* **9**, 2691 (2022).
142. L. Lu *et al.*, "Low temperature sensitivity on-chip Fourier-transform spectrometer based on dual-layer $Si_3N_4$ spiral waveguides," *Photonics Res.* **11**, 591 (2023).
143. X. Long *et al.*, "High-resolution on-chip spatial heterodyne Fourier transform spectrometer based on artificial neural network and PCSBL reconstruction algorithm," *Opt. Express* **31**, 33608 (2023).
144. M. N. Amin *et al.*, "Multi-mode interference waveguide chip-scale spectrometer," *APL Photonics* **9**, 100802 (2024).
145. J. Choi *et al.*, "Inversely designed compact 12-channel mode decomposition spectrometer for on-chip photonics," *ACS Photonics* **12**, 1849 (2025).
146. Y. Li *et al.*, "Inverse-designed linear coherent photonic networks for high-resolution spectral reconstruction," *ACS Photonics* **10**, 1012 (2023).
147. A. Li *et al.*, "An integrated single-shot spectrometer with large bandwidth-resolution ratio and wide operation temperature range," *PhotoniX* **4**, 29 (2023).
148. Z. Zhang *et al.*, "Single-shot on-chip diffractive speckle spectrometer with high spectral channel density," *Laser Photonics Rev.* **19**, 2401987 (2025).
149. E. Le Coarer *et al.*, "Wavelength-scale stationary-wave integrated Fourier-transform spectrometry," *Nat. Photonics* **1**, 473 (2007).
150. X. Nie *et al.*, "CMOS-compatible broadband co-propagative stationary Fourier transform spectrometer integrated on a silicon nitride photonics platform," *Opt. Express* **25**, A409 (2017).
151. F. Thomas *et al.*, "Expanding sampling in a SWIFTS-Lippmann spectrometer using an electro-optic Mach-Zehnder modulator," in *Integrated Optics: Physics and Simulations II*, Vol. **9516** (SPIE, 2015), p. 73.
152. M. J. Grotevent *et al.*, "Integrated photodetectors for compact Fourier-transform waveguide spectrometers," *Nat. Photonics* **17**, 59 (2023).
153. D. Pohl *et al.*, "An integrated broadband spectrometer on thin-film lithium niobate," *Nat. Photonics* **14**, 24 (2020).
154. X. Chen *et al.*, "Dual tunable MZIs stationary-wave integrated Fourier transform spectrum detection," *Sensors* **21**, 2352 (2021).
155. J. Zhang *et al.*, "Cascaded nanobeam spectrometer with high resolution and scalability," *Optica* **9**, 517 (2022).

156. Y. Zhao *et al.*, "Miniaturized computational spectrometer based on two-photon absorption," *Optica* **11**, 399 (2024).
157. S. Zhang *et al.*, "Demonstration of silicon on-chip spectrometer using a racetrack resonator and a mach-zehnder lattice filter," in *2024 Conference on Lasers and Electro-Optics (CLEO)* (IEEE, 2024), p. 1.
158. T. Yang *et al.*, "On-chip optical spectrometer with a tunable micro-ring resonator and a mach-zehnder interferometer lattice filter," *Opt. Express* **33**, 639 (2025).
159. B. B. Kyotoku, L. Chen, and M. Lipson, "Sub-nm resolution cavity enhanced micro-spectrometer," *Opt. Express* **18**, 102 (2010).
160. S. Zheng *et al.*, "A single-chip integrated spectrometer via tunable microring resonator array," *IEEE Photonics J.* **11**, 1 (2019).
161. Z. Zhang *et al.*, "Integrated scanning spectrometer with a tunable micro-ring resonator and an arrayed waveguide grating," *Photonics Res.* **10**, A74 (2022).
162. L. Zhang *et al.*, "Silicon photonic spectrometer with multiple customized wavelength bands," *Photonics Res.* **12**, 1016 (2024).
163. L. Jin, M. Li, and J.-J. He, "Highly-sensitive silicon-on-insulator sensor based on two cascaded micro-ring resonators with vernier effect," *Opt. Commun.* **284**, 156 (2011).
164. P. Sanati *et al.*, "Label-free biosensor array comprised of Vernier microring resonator and 3× 3 optical coupler," *Eur. Phys. J. Plus* **135**, 1 (2020).
165. M. Fujita and T. Baba, "Proposal and finite-difference time-domain simulation of whispering gallery mode microgear cavity," *IEEE J. Quantum Electron.* **37**, 1253 (2001).
166. H. Xu *et al.*, "Integrated single-resonator spectrometer beyond the free-spectral-range limit," *ACS Photonics* **10**, 654 (2023).
167. J. Li, D.-F. Lu, and Z.-M. Qi, "Miniature Fourier transform spectrometer based on wavelength dependence of half-wave voltage of a $LiNbO_3$ waveguide interferometer," *Opt. Lett.* **39**, 3923 (2014).
168. H. Yao *et al.*, "On-chip Fourier transform spectrometer on thin film lithium niobate," *J. Lightwave Technol.* **42**, 6850 (2024).
169. M. C. Souza *et al.*, "Fourier transform spectrometer on silicon with thermo-optic non-linearity and dispersion correction," *Nat. Commun.* **9**, 665 (2018).
170. M. Montesinos-Ballester *et al.*, "On-chip Fourier-transform spectrometer based on spatial heterodyning tuned by thermo-optic effect," *Sci. Rep.* **9**, 14633 (2019).
171. C. Wei *et al.*, "Mid-infrared SOI waveguide thermo-optic Fourier-transform spectrometer," in *Silicon Photonics XVIII*, Vol. **12426** (SPIE, 2023), p. 82.
172. A. Fathy *et al.*, "On-chip parallel Fourier transform spectrometer for broadband selective infrared spectral sensing," *Microsyst. Nanoeng.* **6**, 10 (2020).
173. A. Li and Y. Fainman, "Integrated silicon Fourier transform spectrometer with broad bandwidth and ultra-high resolution," *Laser Photonics Rev.* **15**, 2000358 (2021).
174. R. A. Soref *et al.*, "On-chip digital Fourier-transform spectrometer using a thermo-optical Michelson grating interferometer," *J. Lightwave Technol.* **36**, 5160 (2018).
175. F. Pavanello *et al.*, "Broadband digital Fourier transform spectrometer for on-chip wavelength monitoring in the 2.3-μm wavelength range," *IEEE Photonics J.* **11**, 1 (2019).
176. D. M. Kita, C. Ríos, and J. Hu, "Performance optimization strategies for nanophotonic digital Fourier transform spectrometers," in *Fourier Transform Spectroscopy* (Optica Publishing Group, 2019), p. FTu4B–5.
177. J. Du *et al.*, "High-resolution on-chip Fourier transform spectrometer based on cascaded optical switches," *Opt. Lett.* **47**, 218 (2022).
178. H. Sun, Q. Qiao, C. Lee *et al.*, "Chip-scale mid-infrared digitalized computational spectrometer powered by silicon photonics MEMS technology," *Photonics Nanostruct. Fundam. Appl.* **58**, 101231 (2024).
179. D. Yi *et al.*, "Integrated multimode waveguide with photonic lantern for speckle spectroscopy," *IEEE J. Quantum Electron.* **57**, 1 (2020).
180. M. Harwit and N. J. Sloan, *Hadamard Transform Optics* (Academic Press, 1979).
181. A. Li *et al.*, "An inversely designed integrated spectrometer with reconfigurable performance and ultra-low power consumption," *Opto-Electron. Adv.* **7**, 240099 (2024).
182. D. Yi and H. K. Tsang, "High-resolution and broadband two-stage speckle spectrometer," *J. Lightwave Technol.* **40**, 7969 (2022).
183. C. Yao *et al.*, "Broadband picometer-scale resolution on-chip spectrometer with reconfigurable photonics," *Light Sci. Appl.* **12**, 156 (2023).
184. Z. Zhang *et al.*, "Scalable on-chip diffractive speckle spectrometer with high spectral channel density," *Light Sci. Appl.* **14**, 130 (2025).
185. S.-W. Wang *et al.*, "Concept of a high-resolution miniature spectrometer using an integrated filter array," *Opt. Lett.* **32**, 632 (2007).
186. J. Bao and M. G. Bawendi, "A colloidal quantum dot spectrometer," *Nature* **523**, 67 (2015).
187. J. K. Poon *et al.*, "Silicon photonics for the visible and near-infrared spectrum," *Adv. Opt. Photonics* **16**, 1 (2024).
188. V. Singh *et al.*, "Mid-infrared materials and devices on a Si platform for optical sensing," *Sci. Technol. Adv. Mater.* **15**, 014603 (2014).
189. D. T. Spencer *et al.*, "Integrated waveguide coupled si3n4 resonators in the ultrahigh-Q regime," *Optica* **1**, 153 (2014).
190. P. Cheben *et al.*, *Echelle and Arrayed Waveguide Gratings for WDM and Spectral Analysis*, Vol. **6** (SPIE, 2008).
191. W. Bogaerts *et al.*, "Silicon microring resonators," *Laser Photonics Rev.* **6**, 47 (2012).
192. D. M. Kita *et al.*, "High-performance and scalable on-chip digital Fourier transform spectroscopy [supplementary material]," *Nat. Commun.* **9**, 4405 (2018).
193. A. Herrero-Bermello *et al.*, "Temperature dependence mitigation in stationary Fourier-transform on-chip spectrometers," *Opt. Lett.* **42**, 2239 (2017).
194. D. Melati *et al.*, "Athermal echelle grating filter in silicon-on-insulator using a temperature-synchronized input," *Opt. Express* **26**, 28651 (2018).
195. A. Hänsel and M. J. Heck, "Opportunities for photonic integrated circuits in optical gas sensors," *J. Phys.* **2**, 012002 (2020).
196. K. B. Beć, J. Grabska, and C. W. Huck, "Near-infrared spectroscopy in bio-applications," *Molecules* **25**, 2948 (2020).
197. D. Sanchez *et al.*, "Waveguide-enhanced Raman sensors for bioprocess monitoring," in *Emerging Applications in Silicon Photonics IV*, Vol. **12794** (SPIE, 2023), p. 32.
198. D. Sanchez *et al.*, "Waveguide Raman sensing for chemical detection in industrial processes," in *Optical Fiber Communication Conference* (Optica Publishing Group, 2024), p. M4B–3.
199. W. R. de Araujo *et al.*, "Portable analytical platforms for forensic chemistry: a review," *Anal. Chim. Acta* **1034**, 1 (2018).
200. M. C. Estevez, M. Alvarez, and L. M. Lechuga, "Integrated optical devices for lab-on-a-chip biosensing applications," *Laser Photonics Rev.* **6**, 463 (2012).
201. A. Z. Subramanian *et al.*, "Silicon and silicon nitride photonic circuits for spectroscopic sensing on-a-chip," *Photonics Res.* **3**, B47 (2015).
202. M. R. Bryan *et al.*, "Biosensing with silicon nitride microring resonators integrated with an on-chip filter bank spectrometer," *ACS Sens.* **8**, 739 (2023).
203. K. M. Yoo *et al.*, "Lab-on-a-chip optical biosensor platform: a micro-ring resonator integrated with a near-infrared Fourier transform spectrometer," *Opt. Lett.* **48**, 5371 (2023).
204. Z. Han *et al.*, "On-chip mid-infrared gas detection using chalcogenide glass waveguide," *Appl. Phys. Lett.* **108**, 141106 (2016).

205. M. S. Luchansky and R. C. Bailey, "High-Q optical sensors for chemical and biological analysis," *Anal. Chem.* **84**, 793 (2012).
206. A. Dhakal *et al.*, "Evanescent excitation and collection of spontaneous Raman spectra using silicon nitride nanophotonic waveguides," *Opt. Lett.* **39**, 4025 (2014).
207. A. Dhakal *et al.*, "Nanophotonic waveguide enhanced Raman spectroscopy of biological submonolayers," *ACS Photonics* **3**, 2141 (2016).
208. D. M. Kita, J. Michon, and J. Hu, "A packaged, fiber-coupled waveguide-enhanced Raman spectroscopic sensor," *Opt. Express* **28**, 14963 (2020).
209. J. Michon, D. Kita, and J. Hu, "Sensitivity comparison of free-space and waveguide Raman for bulk sensing," *JOSA B* **37**, 2012 (2020).
210. T. Hu *et al.*, "Silicon photonic platforms for mid-infrared applications," *Photonics Res.* **5**, 417 (2017).
211. L. Ranno *et al.*, "Crown ether decorated silicon photonics for safeguarding against lead poisoning," *Nat. Commun.* **15**, 3820 (2024).
212. "Creative commons attribution 4.0 International Public License," https://creativecommons.org/licenses/by/4.0/ (Date accessed: April 2nd, 2025).
213. L. Tombez *et al.*, "Methane absorption spectroscopy on a silicon photonic chip," *Optica* **4**, 1322 (2017).
214. Z. Dong *et al.*, "Optical performance monitoring: a review of current and future technologies," *J. Lightwave Technol.* **34**, 525 (2015).
215. M. Svaluto Moreolo *et al.*, "Synergy of photonic technologies and software-defined networking in the hyperconnectivity era," *J. Lightwave Technol.* **37**, 3902 (2019).
216. R. Casellas *et al.*, "Photonic device programmability in support of autonomous optical networks," *J. Opt. Commun. Netw.* **16**, D53 (2024).
217. L. Velasco *et al.*, "Monitoring and data analytics for optical networking: benefits, architectures, and use cases," *IEEE Netw.* **33**, 100 (2019).
218. D. Wang *et al.*, "Digital twin of optical networks: a review of recent advances and future trends," *J. Lightwave Technol.* **42**, 4233 (2024).
219. V. I. Tolstikhin *et al.*, "Monolithically integrated optical channel monitor for DWDM transmission systems," *J. Lightwave Technol.* **22**, 146 (2004).
220. T. Ohyama *et al.*, "Compact AWG-based optical channel monitor (OCM) for multi-degree ROADM," in *LEOS 2007-IEEE Lasers and Electro-Optics Society Annual Meeting Conference Proceedings* (IEEE, 2007), p. 167.
221. A. Amrani *et al.*, "Performance monitor for all-optical networks based on homodyne spectroscopy," *IEEE Photonics Technol. Lett.* **12**, 1564 (2000).
222. M. Hasan *et al.*, "High-resolution $Si_3N_4$ spectrometer: architecture & virtual channel synthesis and experimental demonstration," *Opt. Express* **32**, 8697 (2024).
223. M. Bouda *et al.*, "Accurate prediction of quality of transmission based on a dynamically configurable optical impairment model," *J. Opt. Commun. Netw.* **10**, A102 (2018).
224. W. Drexler and J. G. Fujimoto, *Optical Coherence Tomography: Technology and Applications* (Springer, 2015).
225. E. A. Rank *et al.*, "Toward optical coherence tomography on a chip: in vivo three-dimensional human retinal imaging using photonic integrated circuit-based arrayed waveguide gratings," *Light Sci. Appl.* **10**, 6 (2021).
226. E. A. Rank *et al.*, "Miniaturizing optical coherence tomography," *Translational Biophotonics* **4**, e202100007 (2022).
227. G. Yurtsever *et al.*, "Integrated photonic circuit in silicon on insulator for Fourier domain optical coherence tomography," in *Optical Coherence Tomography and Coherence Domain Optical Methods in Biomedicine XIV*, Vol. **7554** (SPIE, 2010), p. 140.
228. B. Akca *et al.*, "Miniature spectrometer and beam splitter for an optical coherence tomography on a silicon chip," *Opt. Express* **21**, 16648 (2013).
229. X. Ji *et al.*, "On-chip tunable photonic delay line," *APL Photonics* **4**, 090803 (2019).
230. X. Ji *et al.*, "Millimeter-scale chip–based supercontinuum generation for optical coherence tomography," *Sci. Adv.* **7**, eabg8869 (2021).
231. B. I. Akca *et al.*, "Toward spectral-domain optical coherence tomography on a chip," *IEEE J. Sel. Top. Quantum Electron.* **18**, 1223 (2011).
232. V. D. Nguyen *et al.*, "Spectral domain optical coherence tomography imaging with an integrated optics spectrometer," *Opt. Lett.* **36**, 1293 (2011).
233. R. M. Ruis *et al.*, "Decreasing the size of a spectral domain optical coherence tomography system with cascaded arrayed waveguide gratings in a photonic integrated circuit," *IEEE J. Sel. Top. Quantum Electron.* **25**, 1 (2018).
234. A. Agneter *et al.*, "CMOS optoelectronic spectrometer based on photonic integrated circuit for in vivo 3D optical coherence tomography," *PhotoniX* **5**, 31 (2024).
235. P. Gatkine, S. Veilleux, and M. Dagenais, "Astrophotonic spectrographs," *Appl. Sci.* **9**, 290 (2019).
236. S. Minardi, R. Harris, and L. Labadie, "Astrophotonics: astronomy and modern optics," *Astron. Astrophys. Rev.* **29**, 6 (2021).
237. J. Bland-Hawthorn and A. Horton, "Instruments without optics: an integrated photonic spectrograph," in *Ground-based and Airborne Instrumentation for Astronomy*, Vol. **6269** (SPIE, 2006), p. 224.
238. S. Shaklan and F. Roddier, "Coupling starlight into single-mode fiber optics," *Appl. Opt.* **27**, 2334 (1988).
239. N. Jovanovic *et al.*, "Efficiently feeding single-mode fiber photonic spectrographs with an extreme adaptive optics system: on-sky characterization and preliminary spectroscopy," in *Ground-based and Airborne Instrumentation for Astronomy VI*, Vol. **9908** (SPIE, 2016), p. 196.
240. J. Bland-Hawthorn and S. G. Leon-Saval, "Astrophotonics: molding the flow of light in astronomical instruments," *Opt. Express* **25**, 15549 (2017).
241. N. Cvetojevic *et al.*, "Characterization and on-sky demonstration of an integrated photonic spectrograph for astronomy," *Opt. Express* **17**, 18643 (2009).
242. N. Cvetojevic *et al.*, "Developing arrayed waveguide grating spectrographs for multi-object astronomical spectroscopy," *Opt. Express* **20**, 2062 (2012).
243. P. Fellgett, "I. - les principes généraux des méthodes nouvelles en spectroscopie interférentielle - A propos de la théorie du spectromètre interférentiel multiplex," *J. Phys. Radium* **19**, 187 (1958).
244. G. Chen *et al.*, "High-speed photodetectors on silicon photonics platform for optical interconnect," *Laser Photonics Rev.* **16**, 2200117 (2022).
245. C. Liu *et al.*, "Silicon/2D-material photodetectors: from near-infrared to mid-infrared," *Light Sci. Appl.* **10**, 123 (2021).
246. J. Michel, J. Liu, and L. C. Kimerling, "High-performance Ge-on-Si photodetectors," *Nat. Photonics* **4**, 527 (2010).
247. F. Ceccarelli, G. Acconcia, A. Gulinatti *et al.*, "Recent advances and future perspectives of single-photon avalanche diodes for quantum photonics applications," *Adv. Quantum Technol.* **4**, 2000102 (2021).
248. N. Na *et al.*, "Room temperature operation of germanium–silicon single-photon avalanche diode," *Nature* **627**, 295 (2024).
249. A. Govdeli *et al.*, "Room-temperature waveguide-coupled silicon single-photon avalanche diodes," *npj Nanophotonics* **1**, 2 (2024).
250. M. Cho *et al.*, "Effective leakage current reduction in GaN ultraviolet avalanche photodiodes with an ion-implantation isolation method," *IEEE Trans. Electron Devices* **68**, 2759 (2021).

251. S. Yanikgonul *et al.*, "Integrated avalanche photodetectors for visible light," *Nat. Commun.* **12**, 1834 (2021).
252. B. Wang and J. Mu, "High-speed Si-Ge avalanche photodiodes," *PhotoniX* **3**, 8 (2022).
253. Y. Alimi *et al.*, "InSb avalanche photodiodes on GaAs substrates for mid-infrared detection," *IEEE Trans. Electron Devices* **67**, 179 (2019).
254. D. Chen *et al.*, "Photon-trapping-enhanced avalanche photodiodes for mid-infrared applications," *Nat. Photonics* **17**, 594 (2023).
255. C.-H. Fann *et al.*, "Novel parallel digital optical computing system (DOC) for generative AI," in *2024 IEEE International Electron Devices Meeting (IEDM)* (IEEE, 2024), p. 1.
256. C. Adamopoulos *et al.*, "Lab-on-chip for everyone: Introducing an electronic-photonic platform for multiparametric biosensing using standard CMOS processes," *IEEE Open J. Solid-State Circuits Soc.* **1**, 198 (2021).
257. K. D. Hakkel *et al.*, "Integrated near-infrared spectral sensing," *Nat. Commun.* **13**, 103 (2022).